Fall 11-15-2018

INVESTIGATION OF THE FORMATION OF γ'' PRECIPITATES UNDER ION IRRADIATION AND ELEVATED TEMPERATURE ENVIRONMENTS

James R. Pike
University of New Mexico

James Pike

Candidate

Department of Nuclear Engineering

Department

This thesis is approved, and it is acceptable in quality and form for publication:

Approved by the Thesis Committee:

Dr. Osman Anderoglu, Chair

Dr. Stuart Maloy

Dr. Youho Lee

INVESTIGATION OF THE FORMATION OF γ'' PRECIPITATES UNDER ION IRRADIATION AND ELEVATED TEMPERATURE ENVIRONMENTS

BY

JAMES RICHARD PIKE

B.S NUCLEAR ENGINEERING, UNIVERSITY OF NEW MEXICO, 2016

THESIS

Submitted in Partial Fulfillment of the

Requirements for the Degree of

Master of Science

Nuclear Engineering

The University of New Mexico

Albuquerque, New Mexico

December, 2018

DEDICATION

I would like to dedicate this to my family for the support, encouragement and wisdom they have shared with me throughout life. I consider myself to be very fortunate to have the loving support from my family.

ACKNOWLEDGEMENTS

I would like to thank my colleagues – Paul, Deep, Carly, Mehadi, Floren and Phoenix – for their support, wisdom and help on a wide variety of tasks related to my thesis. I would like to thank Dr. Zhang and Dr. Radhakrishan for their TEM help and guidance.

I would like to thank Dr. Anderoglu for providing me an opportunity to join the Xtreme Materials group at UNM. I would like to thank Dr. Maloy from LANL for his guidance and advising my thesis. I would like to thank Eric Olivas from LANL for his guidance on stress analysis of the ion beam window. I would like to thank Dr. Eda Aydogan for twin jet electropolishing my samples. I would like to thank Dr. Lee for his time and contributions in reviewing and advising my thesis research.

I would like to thank Dr. Barr and Dr. Hattar at Sandia Nation Laboratory for their help, guidance and patience in using the *in-situ* ion beam facility. This work was performed, in part, at the Center for Integrated Nanotechnologies, an Office of Science User Facility operated for the U.S. Department of Energy (DOE) Office of Science by Los Alamos National Laboratory (Contract DE-AC52-06NA25396) and Sandia National Laboratories (Contract DE-NA-0003525).

Investigation of the Formation of γ'' Precipitates Under Ion Irradiation and Elevated Temperature Environments

by

James Richard Pike

B.S Nuclear Engineering, University of New Mexico, 2016

ABSTRACT

During a preventative maintenance at the Los Alamos Neutron Science Center (LANSCE) Isotope Production Facility (IPF), a beam window made of solution annealed Alloy 718 was replaced and the old beam window was analyzed. The old beam window underwent mechanical testing and microstructure analysis. During the microstructure analysis, the formation of γ'' precipitates was observed in Transmission Electron Microscopy (TEM) electron diffraction pattern. The formation of γ'' precipitates was not expected since they are not stable under irradiation. Furthermore, the formation of γ'' precipitates was observed only at a temperature of 33ºC, and a dose of 0.7 displacement per atom (dpa) with energetic H+ ions. The precipitate formation was not observed in the rest of the analyzed section of the beam window. The present work attempts to explain the formation of the precipitates with a series of carefully designed in-situ irradiation experiments at different doses, dose rates and temperatures.

Testing at Sandia National Laboratory's (SNL) Ion *in situ* TEM lab (I3TEM) was used to investigate the temperature and dose rate that γ'' precipitates will form under

irradiation. The first test was conducted with 1.2 MeV Ni ions at room temperature up to a dose of 1.4 dpa. The test results concluded that γ" precipitates do not form under high dose rates (compared to protons in the actual beam window). The second test was conducted using 2.8 MeV Au ions at 200 ºC and came up with the same null findings. The test concluded elevated temperatures and irradiation conditions do not foster an environment for precipitation growth. A third and final test to investigate phase stability in solution annealed Alloy 718 was conducted using 800 KeV H+ ion irradiations and concluded that the γ" precipitates do not form under slower irradiation doses either.

Investigation into energy deposition using The Stopping and Range of Ions in Matter (SRIM) to compare the formation energy to deposited energy of γ" precipitates was performed. The energy deposited compared to the formation energy was used to conclude there was no correlation.

The stress state of the material under influence of the ion beam under normal operations was simulated with finite element analysis using Solidworks. The simulation showed that the maximum stress was located in the same outer region where the γ" precipitates were discovered. Furthermore, the stress levels were found to be similar to literature work. Therefore, the formation of γ" precipitates in the solution annealed beam window of LANCE Isotope Production Facility could be attributed to stress. Further studies could find a balance between irradiation induced disordering and stress induced formation.

TABLE OF CONTENTS

LIST OF FIGURES

LIST OF TABLES

CHAPTER 1: INTRODUCTION

The need to find a sustainable, easily accessible, reliable and clean energy source is critical for the economic growth of the world [1]. Future designs of nuclear reactors call for operations at higher temperatures and higher neutron dose rates. In addition, the materials must also withstand very corrosive coolants and internal stresses. A limiting factor to some new reactor designs has been finding a suitable materials to withstand the extreme environment. In a nuclear reactor, materials serve many different purposes in many different environments. Choosing the correct material prompts many challenges for research and commercial use [1–10].Since the 1950's, many reactor designs have been introduced. During the last 70 years, reactor designs have been improved to reflect on current safety issues and to ensure a more economical reactor. Figure 1 shows the advancement of reactors. The future generation of Gen-IV reactors is expected to operate at higher temperatures and dose rates. Gen IV reactors are being designed to be more safe and economical than previous Gen III reactors [9].

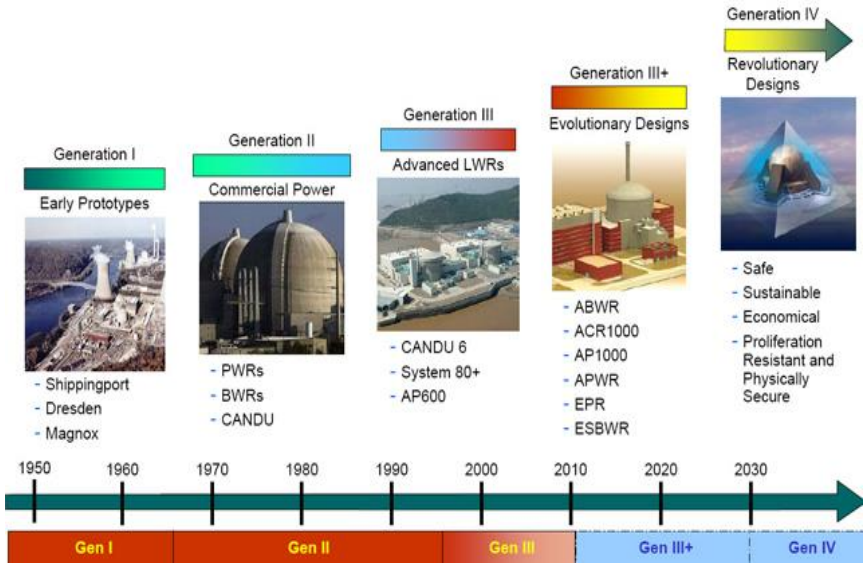

Figure 1. The progression and future of nuclear reactors.

There are six initial reactor designs used for producing nuclear power around the world [11]. The main six designs are Magnox, Pressurize Water Reactor (PWR), Boiling Water Reactor (BWR), Pressurize Heavy Water Reactor (CANDU), Advanced Gas Cooled Reactors (AGR) and the Russian's RBMK reactor. The British's Magnox reactor design is a gas cooled, graphite moderated reactors that used magnesium cladding with a uranium metal fuel. The British then went on to improve the Magnox design, AGR, to include uranium dioxide (UO_2) fuel pellets to increase thermal efficiencies. The Russian's RBMK reactor is a graphite moderated, water cooled reactor with UO_2 pellets as fuel. The CANDU is a heavy water moderated reactor that used naturally enrich UO_2 fuel pellets. BWR and PWR use UO_2 fuel pellets with zirconium cladding and are classified as Light Water Reactors (LWR). The operating temperatures of the most commercial reactors are around 300 ºC except for AGR designs which can go up to 650 ºC [11]. The change in coolant temperature across the core is around 40-50 ºC. Dose rates for structural materials in LWRs

can reach 100 displacement per atom (dpa) towards the end of the reactors life [10]. Dpa is the universally accepted magnitude of a unit of dose to a material. The unit represents the number of times that all atoms are displaced from their original position. For instance, 1 dpa means on average every atom is displaced from it is lattice position at least once. Extensive research has been conducted into current materials inside the commercial reactors [12–14]. The materials currently being used in commercial reactors are not feasible for some of future reactors designs.

The current design for a PWR has many material components that need to work in harmony with each other and not fail. Figure 2 shows the range of materials that are found in a nuclear reactor.

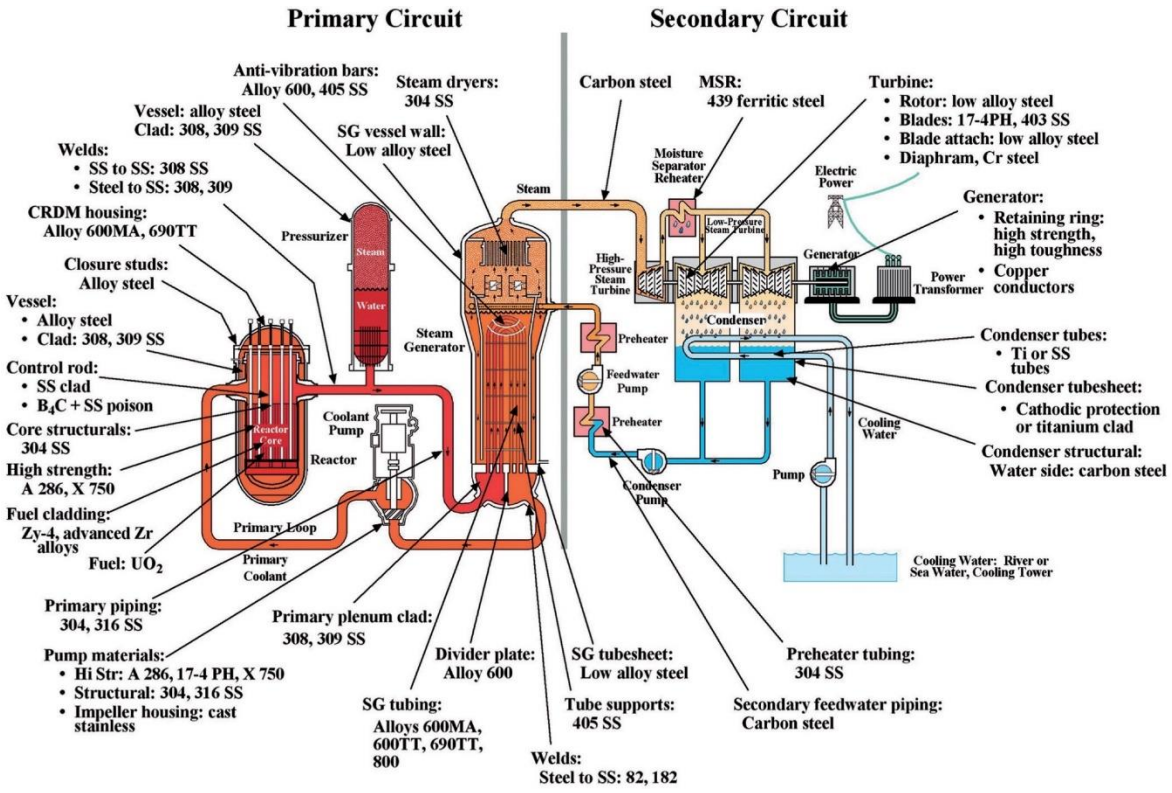

Figure 2. Schematic of PWR with materials at each part of the system [4].

The structural materials in a reactor operates at 300 ºC for upwards of 50 years. During the lifetime the material can crack, oxidize, and corrode. In addition, the synergistic effects of multiple degradation mechanisms is also possible. For instance, stress corrosion cracking is one of the well-known problems currently being studied.

Future upgrades to LWRs include researching and implementing accident tolerant fuels (ATF) into current systems. ATF are fuels that have an enhanced accident tolerance compared to the standard UO_2 – Zirconium cladding systems while keeping or improving on fuel performance [15–17]. To be a viable ATF candidate, one or more of the following attributes need to be satisfied in comparison with zircaloy cladding: reduced hydrogen generation rate, increased fission product retention, improved (reduced) reaction kinetics with steam, improved fuel and cladding properties (e.g. high temperature strength, corrosion resistance in water). Improved properties also include high melting point and higher thermal conductivity [17]. ATFs must go through a very thorough safety test before being implemented into current LWRs. Considerations for economic and fuel cycle impacts are heavily taken into consideration.

The extreme environments of future nuclear reactors designs have resulted in challenges to find materials to uphold to these extreme environments. Figure 3 shows the temperature and dose challenges of the future reactor designs.

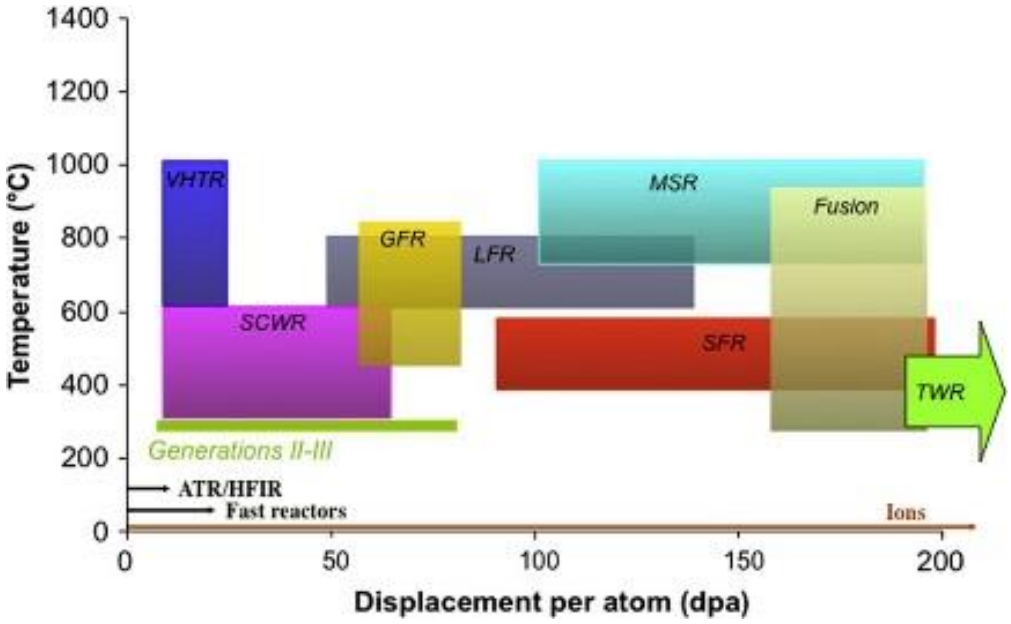

Figure 3. Challenges of future Gen-IV reactors in terms of temperature and dose [4].

Current reactors on the market are Gen II, Gen III and Gen III+ designs. The United States currently has 100 reactors; 65 PWRs and 35 BWRs. The future Gen IV reactor designs, include super critical water-cooled reactor (SCWR), lead fast reactor (LFR), molten salt reactor (MSR), gas-cooled fast reactor (GFR), very high temperature reactor (VHTR), and sodium fast reactors (SFR) [4].

SCWR's are essentially LWR's that operate at a pressure higher than 22.1 MPa [18]. LFRs use lead as a coolant and operate in a fast neutron spectrum through using a liquid metal coolant (rather than water). The fast neutron spectrum is related to the energy of the neutron created from fission. Fast neutrons have an energy greater than 1 keV and

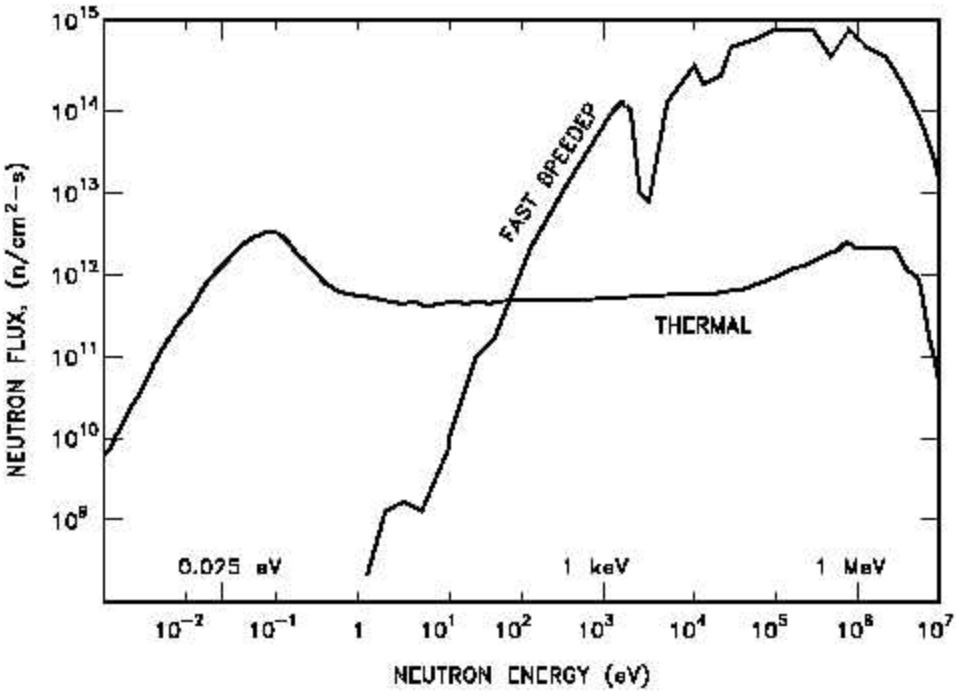

Figure 2. Neutron Energy Spectrum for a Thermal and Fast Breeder Reactor [71]

thermal neutrons have an energy less than 1 eV [19].

MSRs use molten fluoride salt as fuels and coolant. The operating temperatures of MSRs are around 700 ºC [20] and can reach dose rates in the core of up to 200 dpa [9]. GFRs are similar to AGR and RBMK but the reactor operates in the fast neutron spectrum. The future operating temperature range of Gen-IV GFRs is between 450-850 ºC [21]. VHTRs use helium as a coolant and can reach up to 1000 ºC [5,21]. VHTRs are thermal reactors and are expected to have an estimated lower dose of around 10 dpa, at end of life

to surrounding materials. SFR's use sodium as its coolant and operate in the fast neutron spectrum.

The future Gen-IV reactors operate at in a more extreme environment than previous generation reactors. Gen-IV reactors are considering new styles of fuel, coolants, fast neutron spectrum and higher temperatures. One design for fuels of GFRs uses coated fuel particles packed in graphite structure. The coated fuel particles contain a SiC layer to retain fission products and to provide structural support. The fuel particle faces the challenge of operating without failure in the environment of high temperatures and high neutron fluxes. Coolants for future Gen-IV reactors create highly corrosive environments. Lead and lead alloys are being consider as coolants. A challenge with lead is solubility of Fe, Cr, and Ni elements [5]. The solubility of elements abundant in most alloys creates challenge for corrosion protection in lead systems. Limited fast test reactors create bottlenecks for further testing on how a material will react under a fast neutron spectrum. Research time is limited in the fast test reactors. High temperatures create a large change in temperature (ΔT) across the reactor core. Gen -IV reactors are expected to have a ΔT of around 300-400 ºC with some designs having a ΔT of 500 ºC [9]. Material properties can change significantly over this large range of temperatures. Finding a material that could withstand a large ΔT, fast neutron spectrum and corrosive coolants is a challenging task.

Under irradiation, a material can undergo microstructural changes which lead to significant changes in material properties. When a material is in a neutron environment, energetic neutrons can knock an atom out of its lattice position. The displacement of atoms with sufficient energy creates more point defect pairs (Frenkel pairs) in cascades and eventually can create defect clusters such as voids, and dislocation loops. The radiation

damage mechanism is discussed in more detail together with quantification in the next chapter. The accumulation of voids can cause significant swelling. Figure 4 shows void swelling of materials.

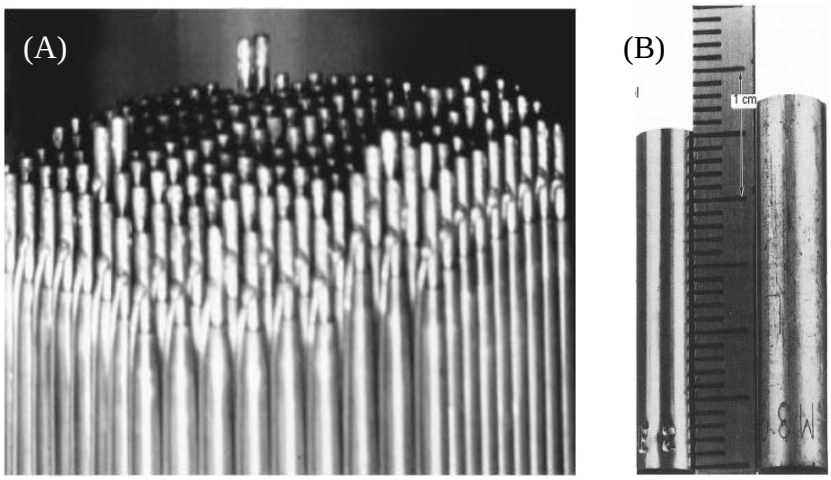

Figure 3 Void swelling of SS 316 [4]

Materials can experience radiation hardening and loss of ductility. Radiation can induce precipitates, disordering and cause dissolution. An example of radiation induced precipitates is Ni-Si system [22]. Radiation damage causes the typical vacancies, voids and interstitials to form. The small Si atoms defuse to sinks and creates Ni_3Si precipitates.

The study of materials at the micro, nano and atomic scale are important to establish microstructure-physical property relations. As a result, employing micro, nano, and atomic techniques to nuclear materials has proven to be very important [6]. Techniques, such as, scanning electron microscopy (SEM), focus ion beam (FIB) analysis, transmission electron microscopy (TEM), small angle neutron scattering (SANS) and atom-probe tomography (APT) are being used to understand the microstructural changes that result in irradiation induced embrittlement, corrosion, segregation at grain/phase boundaries. APT works by using a cryogenically-cooled needle shape specimen with a radius of about 50 nm. A laser is then pulsed on to the specimen removing ions which then travel to a sub-nano resolution

detector. The sub-nano resolution detectors can create 2-D and 3-D images. The images produced can show the distribution of particles along a grain boundary and throughout a material [6,23]. Commonly less used SANS and small angle x-ray scattering determine the element and size by the diffraction of the neutron or x-ray. TEM images defects in a material by passing an electron beam through electron transparent material e.g. a sample of a thickness less than ~100 nm. TEM is discuss in greater details in Chapter 3.

Alloy 718, also known as Inconel 718, has been considered as a choice of material for many high strength and corrosion resistance environments. Alloy 718 is a nickel-base super alloy which contains the elements niobium, titanium, aluminum, molybdenum, chromium and balance with iron. Alloy 718 is used in high temperature applications such as jet engine and furnace parts [24]. Schlumberger Technologies used Alloy 718 for high pressure gas wells because of its material properties [25]. Precipitated hardened and solution annealed are two different heat treatments for use of Alloy 718. Precipitation hardened uses a series of annealing temperatures, greater than 700ºC, to form two material strengthening precipitates. The precipitates that form are γ' and γ''. The γ' precipitate is $Ni_3(Al,Ti)$ that forms in a $L1_2$ lattice. The γ'' precipitate is Ni_3Nb that forms a $D0_{22}$ lattice.

In Figure 3, the lattice structures are illustrated. The average volume fraction of γ' and γ" precipitates are 4% and 15% respectively in a precipitation hardened alloy [26].

Alloy 718 is used as a material for cooling pipes and beam windows for a neutron spallation environment [27]. In a spallation environment, very energetic (600-800 MeV) protons collide with the nucleus of a heavy element. The heavy element will undergo a

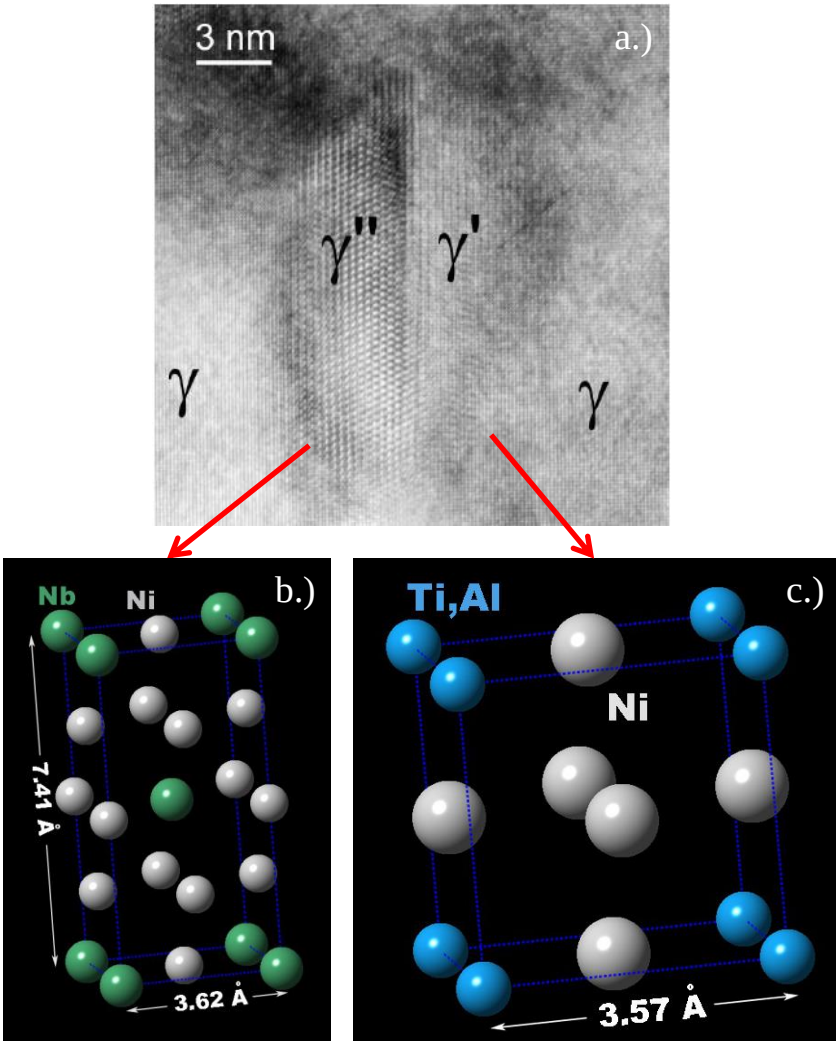

Figure 4. a.) TEM image of γ' and γ" precipitates b.) $D0_{22}$ lattice c.) $L0_2$ lattice

intranuclear cascade and emit neutrons and protons. The heavy element will then go to the evaporation phase and emit more neutrons or protons through a decaying process or fission [28]. The use of Alloy 718 in spallation environment provides information on if Alloy 718

could withstand some of the aforementioned reactor environments. Under thermal reactor conditions, a Ni transmutation interaction can lead to He being produce which at high temperatures and under stress can cause He embrittlement. Alloy 718 is used in irradiated environments such as bolts for a nuclear reactors [29], coolant pipes for spallation environments [27,30] and as a proton beam window [36] for the Los Alamos Neutron Science Center (LANSCE) Isotope Production Facility (IPF). Similar alloy, Inconel X-750, is used as spacers because of strengthening γ' precipitates.

The γ' precipitate has been studied in other nickel base alloys such as Nimonic PE16 [32,33]. Nelson and Bourdeau teams discovered that around 0.1 dpa at room temperature, γ' precipitates becomes disordered. Inconel X-750 γ' precipitate was investigated at a range of temperatures and dpa's by Zhang et al. [34]. Ion irradiations have been used to study γ' and γ'' precipitates of Alloy 718. Sencer et al. studied the precipitate stability after exposure to 600-800 MeV protons and temperatures below 60 ºC. The studies reported that at 0.1 dpa, disordering had occurred [27]. Sencer et al. did another study replicating a spallation environment with high energy protons and neutrons, and found that at 0.6 dpa disordering had occurred [30]. Alloy 718 was studied under electron irradiation at elevated temperatures. The study concluded that at extremely low dose of 0.001 dpa, disordering is possibly happening. Jin et al. investigated the evolution of Alloy 718 precipitates with Kr ions[35]. The test was conducted at 290 ºC and 550 ºC and noted that γ' and γ'' precipitates are easily disordered at 5 dpa.

Stability of both γ' and γ'' precipitates have been studied under neutron irradiation in Alloy 718. Thomas and Bruemmer studied the effects of neutron irradiation on γ' and γ'' precipitates[29]. The study reported that dissolution occurred at about 20 dpa and 3.5 dpa

at a temperature of 288 ºC for both γ' and γ'' precipitates respectively. Thomas and Bruemmer also studied grain boundary elemental segregation and noted that during neutron irradiation nickel diffuses to the grain boundary. The study reported that the hardness of Alloy 718 decreases with increasing dose due to irradiation hardening.

In 2009, Los Alamos Neutron Science Center (LANSCE) Isotope Production Facility (IPF) investigated a beam window as shown in Figure 3. The IPF is capable of making a variety of medical isotopes including Mo-99.

Figure 5. LANSCE Facility at Los Alamos

The investigation was prompted by desire to extend of the lifetime of the window to higher doses without incurring failure [36]. The beam window is crucial as it serves as a barrier between the vacuum and the target protecting the proton beam components, which are kept under vacuum from the coolant in the target chamber. The beam window is 76.2 mm diameter and 0.5 mm thick and made entirely out of solution annealed Alloy 718. Analysis of the beam window included visual, beam profile measurement, thermal, MCNPX and

Transmission Electron Microscopy (TEM) analysis. The samples analyzed from the window experienced irradiation temperatures that ranged from 33 ºC – 100 ºC and ranged in dose rates of 0.2 displacements per atom (dpa) – 10.6 dpa [31].

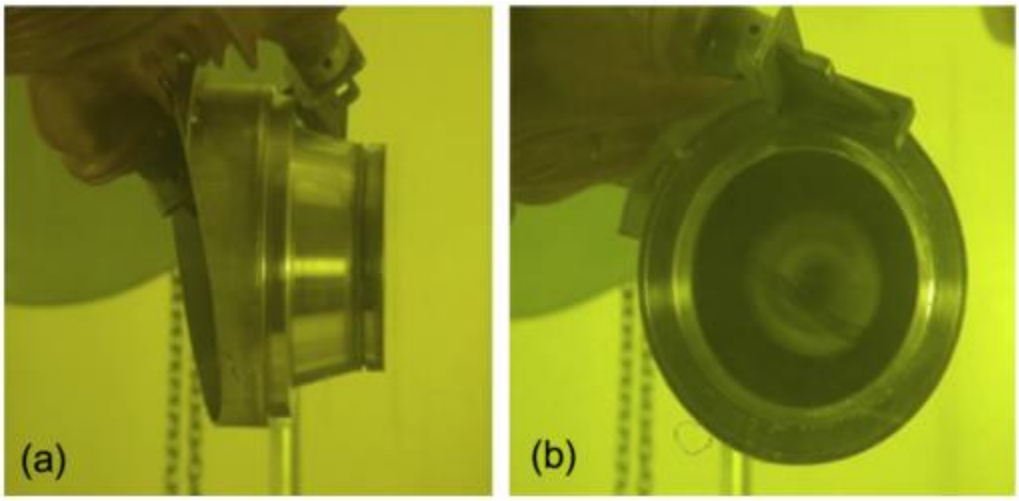

Figure 6. Ion Beam window at LANSCE IPF. (a) side view of alloy 718 beam window. (b) front view of alloy 718 beam window.

During the 2009 investigation of the ion beam window, γ" precipitates were discovered in a sample that had a dose of about 0.7 dpa and at a temperature of 34 ºC [36]. The selected area diffraction (SAD) pattern showed superlattice reflections from the presence of γ" precipitates. The finding of γ" precipitates was unusual because the regions showing the presence of γ" precipitates did not have the highest dose rates or temperature. A increase in shear strength was observed in the same area as the presence of γ" precipitates. The increase of hardness is attributed to the γ" precipitates. Similar increase of hardness have been seen in Byun et al research solution annealed alloy 718 [36]. Byun et al tested SA Alloy 718 up to a dose rate of 1.2 dpa and an estimated temperature range of 60-100 ºC. The temperature was not held constant because the specimens were in direct

contact with the coolant. Post irradiation mechinical properties testing concluded a significant increase in yield strength and ultimate tensile strength. The increase of strength was contributed to defects and no mircostrucure investagation was conducted.

The investigation into Alloy 718 under different ion irradiation and temperature conditions will help us understand the formation of γ' and γ" precipitates. LANL investigation into the ion beam window at LANSCE IPF facility yielded a discovery of γ" precipitates in solution annealed Alloy 718. The facilities at both Los Alamos National Labs and Sandia National Labs (SNL) were used in the investigation of the cause of the formation of γ" precipitates in Alloy 718. Tests at the In Situ Ion Irradiation TEM facility (I3TEM) were performed at SNL. Material preparation of Alloy 718 occurred at LANL where the samples were punched into 3 mm disks and twin jet electropolished.

The research conducted here investigates Alloy 718 under different doses and temperatures to determine conditions that favors the formation of γ" precipitates. The I3TEM facility at SNL was used to map out a diffraction pattern from the TEM every 3 minutes. The test was conducted at room temperature with Ni^{+2} ions and at 200 ºC with Au^{+4} ions. Diffraction patterns showed no indication of any formation of γ" precipitates. In situ proton irradation was done at room temperature at an energy of 800 keV. The total dose rate induced by proton irradation was 0.03 dpa. The test was to simulate the irradiation environment that was experienced at the LANSCE IPF facility. The results concluded no precipate formation was induced by irradiation.

CHAPTER 2: THEORY AND BACKGROUND

2.1 Radiation Damage on Materials

A radiation environment is very harsh and destructive. Radiation can induce defects in materials which can lead to microstructural changes. The microstructural changes result in a change of mechanical properties. The damage done by radiation can also disorder and cause dissolution of existing precipitates. In addition radiation can induce precipitate formation. This chapter will discuss these topics in greater detail.

2.1.1 Defects formed by Radiation Damage

A radiation damage event is defined as the transfer of energy from an incident projectile to the solid and the resulting distribution of target atoms after completion of the event [22]. The damage event is when an energetic ion (or neutron) interacts with a lattice atom. The energetic projectile must have enough energy to displace the atom from the lattice. The minimum energy to displace an atom is called threshold energy or displacement energy. For metals such as Ni, Fe, Cr, the threshold energy is around 40 eV [22]. Once an atom is displaced from its lattice, it is known as a primary knock on atom (PKA). The passage of the initial particle can cause more than one PKA until termination of the particle. The PKAs cause damage cascades which are a collection of point defects. The damage event is concluded when all PKAs and the initial projectile come to a rest.

Defects occur naturally in a material and can also be induced in large quantities by irradiation. The primary radiation induced defects at 0D are vacancies and self-interstitials. A vacancy defect is a missing lattice atom. An interstitial defect is an atom located in a matrix where normally an atom would not have existed. Figure 4 shows how a projectile can cause damage and defects in a material. Vacancies can cluster to form 3-dimensional defects that are called cavities. Cavities can be grouped into two distinct terms, voids and

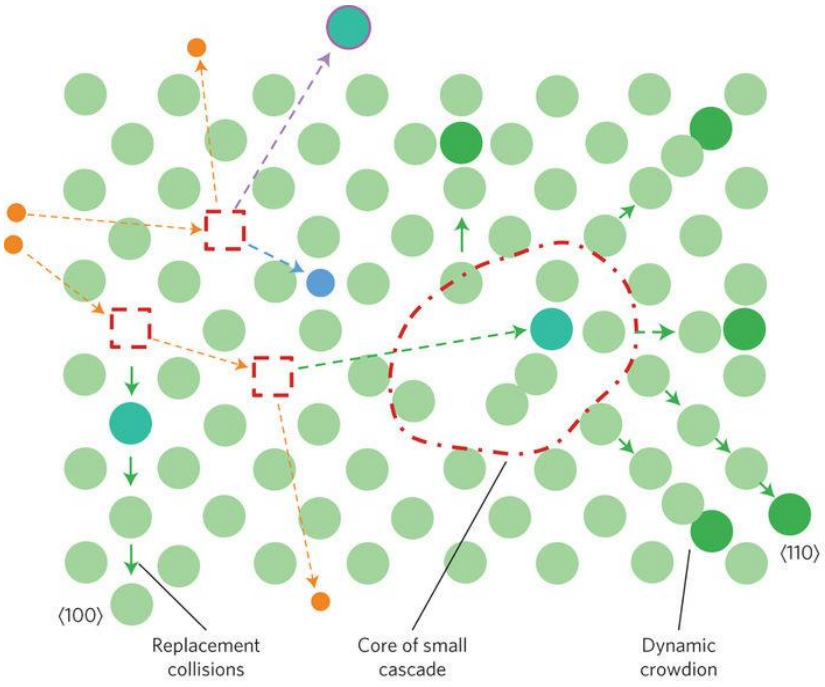

Figure 7. Possible damage events for a projectile entering a material [72].

bubbles. Voids are clusters of vacancies in the absence of gas pressure while bubbles refer to pressurized cavities due to gas atoms such as He. When an atom is knocked out of its lattice position, two defects are created which are called Frenkel pairs. A Frenkel pair is a vacancy and an interstitial. Crowdions and replacement collisions are defects that occur along a line. A replacement defect is when an atom is knocked off its lattice and has enough energy to knock the next atom in line. This defect sequence will last if the energy of the

projectile atom can overcome the displacement energy the next atom in line. A crowdion defect is when an extra atom gets knocked into a line of atoms.

The magnitude of radiation damage is given in terms of displacement per atom (dpa). Dpa is average number of atoms being displaced. A dose of 1 dpa means on average every atom has been displaced once [37]. A simple way of calculating dpa is using the Kinchin-Pease (K-P) method. K-P introduces a step function. If the energy of the incoming particle is less than the displacement energy, E_d, than the number of displaced atoms is 0. If the energy of projectile is between the E_d and $2E_d$ than the number of displaced atoms, $\nu(T)$, is 1. When the projectile energy is greater than $2E_d$ and less than an upper limit, E_c, the formula for displaced atom is shown in Eqn. 1 [22].

$$\nu(T) = \frac{T}{2E_d} \qquad \text{Eqn. 1}$$

E_c is an upper saturation energy when the number of defects being produced is equivalent to defects recombining. If the projectile energy is greater than E_c than the number of atoms displaced follows the equation 2.

$$\nu(T) = \frac{E_c}{2E_d} \qquad \text{Eqn. 2}$$

Modification of K-P model have been made. In 1975, Norgett, Robinson and Torrens modified the K-P equation by proposing a efficiency factor and energy lost in damage cascade term [22]. The Norgett, Robinson and Torrens (NRT) equation is shown below where κ is displacement efficiency, E_D is the total damage and η is energy lost in the cascade by electron excitation.

$$\nu(T) = \frac{\kappa E_d}{2E_d} = \frac{\kappa(T-\eta)}{2E_d} \qquad \text{Eqn. 3}$$

The method on how to calculate dpa in a material will be discussed in detail in Section 2.3.1.

Irradiation temperature play a role in defect mobility and recombination. Agullo-Lopez et al. [38] studied the defect mobility in copper after electron irradiation. The defect mobility and recombination were measured by the induced resistivity of the copper sample. Five recovery stages for materials under temperature are shown in Figure 5. The first stage (I) is at very low temperatures. The dose rate is proportional to defect production up until defects created are being annihilated by preexisting defects earlier in the irradiation. In this

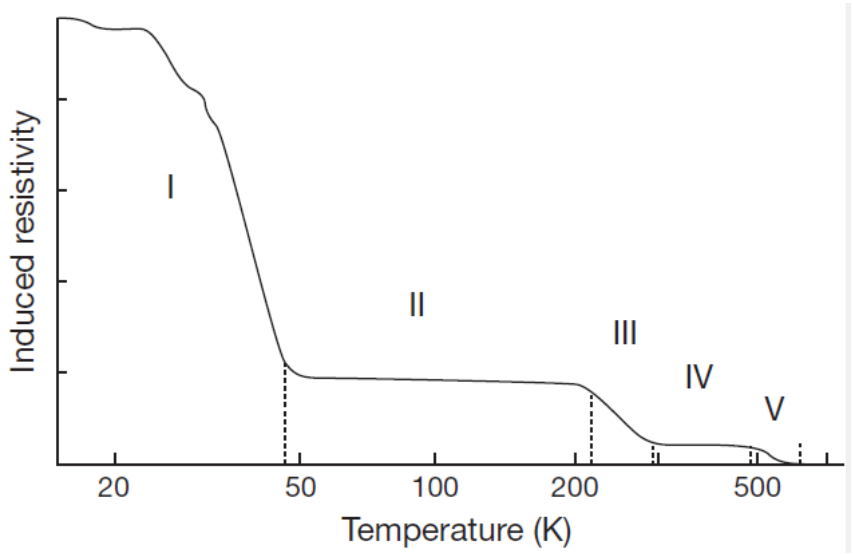

Figure 8 Electrical resistivity of defects and recovery of the defects of copper after electron irradiation [38].

stage mobility of self-interstitials atoms is present but vacancy mobility is almost nonexistent. Self-interstitial atoms can anneal with vacancies in this stage or partly survive by forming interstitial clusters or by being trapped at sinks. In Stage II, self-interstitials clusters are mobile but vacancies are not. Self-interstitial clusters grow by mutual coalescence, a process that continues up to stage V. The self-interstitial clusters may migrate to surface and grain boundary sinks. In alloys, interstitials trapped at foreign atoms in stage I can be detrapped. Stage III is when vacancies become mobile and can either annihilate at interstitial clusters or form vacancy clusters that coarsen in Stage IVStage IV vacancies become even more mobile. Vacancies start to cluster and create voids. Stage V

is about $0.5T_{melt}$ of the temperature. Vacancies cluster start to emit free vacancies which anneal with self-interstitial atoms. Vacancies cluster are mobile enough to migrate and anneal to the surface. As temperature increase defects decrease due to mobility and annealing.

Radiation induced segregation (RIS) is when elements in the material tend to diffuse to or away from a grain boundary. The RIS can lead to lower corrosion resistance and strength of material. Thomas and Bruemmer found RIS in neutron irradiated Alloy 718 [29]. The studied showed a large increase in Ni enrichment and a depletion of Cr and Fe at the grain boundaries.

2.1.1.1 Effect of radiation on material properties

Irradiation environments can affect the strength and ductility of a material. As defects accumulate in a material the strength of a metal alloy tends to increase while the ductility decrease. This increase in hardness due to irradiation is often called radiation induced hardening or irradiation hardening. In some cases, hardness/strength of the material could be reduced by irradiation because of disordering and dissolution of precipitates. The decrease in hardness is called radiation induced softening. PH Alloy 718 has been studied and noted to have radiation induced softening [39]. The radiation induced softening is caused by the disordering and dissolution of γ' and γ'' precipitates found in PH Alloy 718. In the case of SA Alloy 718, it tends to show radiation induced hardening [29,31,40].

Metal alloys which do not experience a loss of precipitates at higher dose rates are prone to see an increase in yield strength (YS) and a significant decrease in elongation. Depending on the material, a dose rate saturation point will be reached were YS and elongation will reach a maximum or minimum, respectively. Defects induced in the material are obstacles to any type of gliding defects. The reduced length in gliding defects causes elongation to decrease. Since the radiation induced defects trap and stop the gliding defects this increases the YS. The gliding defects could include 1, 2 and 3 dimensional

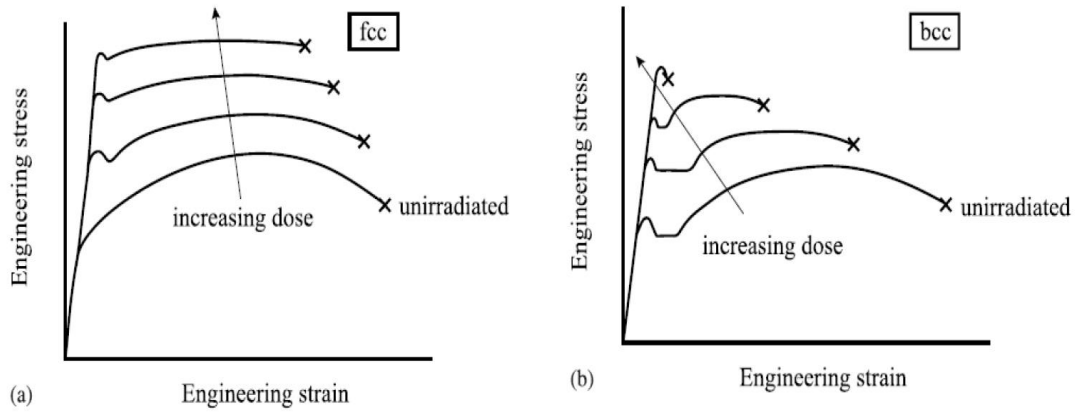

Figure 9 (a) The typical Strain vs. Stress curve for a FCC material under irradaiation. (b) The typical Strain vs. Stress curve for a BCC material under irradaiation. [22].

defects. Face centered cubic (FCC) and body center cubic (BCC) microstructures act differently under irradiation conditions. Both FCC and BCC microstructures experience an increase in yield strength as shown in the figure below. BCC microstructures have less ductility than FCC microstructures because of the packing of BCC microstructures [22]. When materials are deformed, dislocations are produced resulting in deformation by one burgers vector for each dislocations that moves through the lattice. Because BCC materials have reduced atomic packing compared FCC materials less slip systems are available resulting in a reduced elongation. BCC has a lower packing ratio and more areas for interstitials atoms.

2.1.2 Ion Irradiation versus Neutron Irradiation

The use of ions to emulate how a material will act under neutron irradiation has become increasingly popular. Different types of irradiating species can create defects at different orders of magnitude and depth. Ions, electrons and neutrons all cause different damage cascades and penetrate to different depths. Ion irradiation can vary dependent on the atomic weight of the ion and the energy used for the irradiation. Higher Z materials cause larger damage cascades but do not penetrate far into the material. Lower Z material can penetrate further into a material but cannot achieve the damage rate produce by cascades similar to the heavy ions. Ions with the same energy will penetrate different depths in different materials. In a pure silicon matrix, a 1 MeV Ni ion will penetrate about 1 micron compare to 17 microns of a proton of the same energy. Figure 7 shows the depth of Ni ions and protons calculated using the program SRIM. .

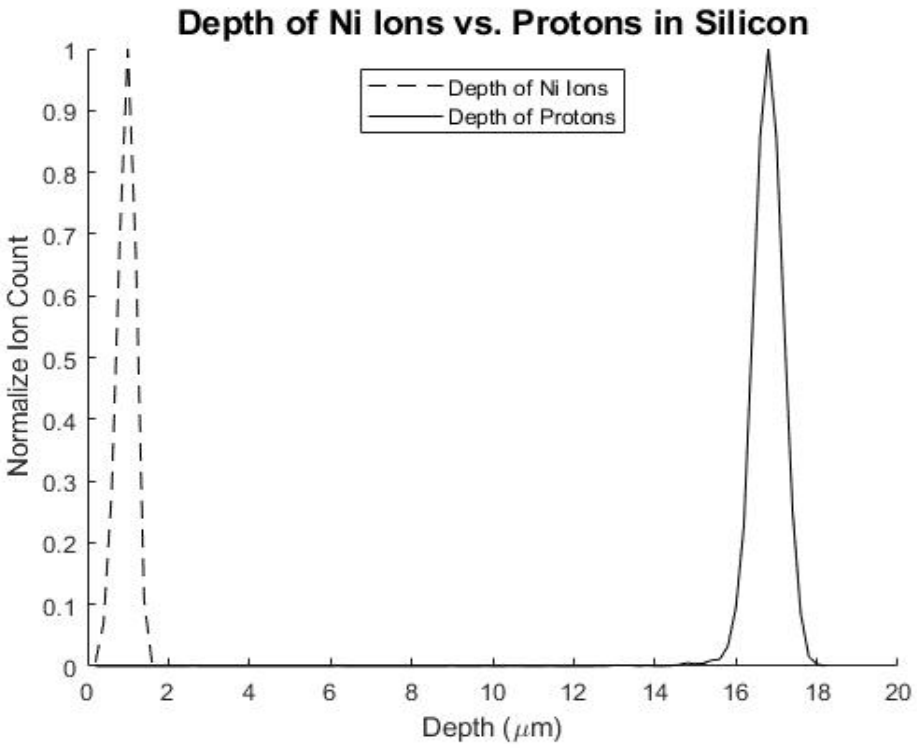

Figure 10. Depth of Ni Ions and Protons in a silicon matrix

. Electrons can create displacements in a material but with very low recoil events [41]. Using electrons to irradiate a material will not cause the same damage as neutrons. Coulomb interaction between electrons and atoms limits the depth an electron can penetrate in a material. Since neutrons have a neutral charge, the slowing down of a neutron is by neutron-nucleus interactions. A neutron has a mean free path in the order of centimeters.

The use of ions to emulate neutron irradiation is a fast and inexpensive compared to neutron irradiations in a reactor. Ion irradiations can be grouped into those performed with light ions and heavy ions. Heavy ions can achieve very high dose rates in a very short amount of time. Heavy ions also produce large cascades which are produced in neutron irradiation. Heavy ions have multiple disadvantages [42]. The main disadvantage is the limited depth the ion will penetrate in a material. A minor disadvantage is a larger increase in temperature due to deposited energy. Light ions are very promising to simulate neutron

irradiation. Light ions still do not penetrate as far as neutrons in a material. Light ions can still cause cascade events and produce moderate dose rates and at reasonable irradiation times. Below is a table to summarize the disadvantages and advantages of ion irradiations versus neutron irradiation.

Table 1. Advantages and disadvantages of ion and electron irradiations vs neutron irradiations

Irradiation Type	Advantages	Disadvantages
Electrons	• High dose rate • Simple Source • In-situ observation	• No cascades • Large temperature shifts compared to neutrons. • No transmutation
Heavy Ions	• Very high dose rate • Short irradiation time • Large cascade production	• Very limited depth • Peak damage profile • Implantation of ion • High dpa rate which cause a higher temperature shift • No transmutation
Light Ions	• Moderate dose rates • Moderated irradiation times • Decent depth of penetration • Flat damage profile for initial part of the depth.	• Smaller cascade • Limited transmutation

2.2 Formation of γ' and γ'' Precipitates

2.2.1 Formation and kinetics of Precipitates

The formation of γ' and γ'' precipitates are noticed under high temperature of about 1400 ºF and long annealing times processes of 15-20 hours. The process of precipitation occurs by the nucleation and growth of precipitates from supersaturated solutions [43]. The growth rate of the precipitates varies based on the nucleation rate and is time dependent. The evolution of the size and distribution of the precipitates is driven by the abundance of

surface energy. The process is also known as coarsening. The formation of precipitates can be described with diffusion theory, Ostwald Ripening and modification to Ostwald ripening such as Lifshitz, Slyozov and Wagner theory (LSW theory). The formation of precipitates have been observed to be enhanced and/or induced from external stress on the material and in irradiation environments.

The diffusion of atoms is driven by six dominant mechanisms. FCC and simple cubic crystalline structures both have vacancies and interstitial diffusion mechanisms. While BCC and hexagonal close-packed materials have only vacancy diffusion mechanisms [22]. Vacancy diffusion is when an atom resides in a lattice next to a vacancy and exchanges places [44]. Interstitial diffusion is the migration of atoms from one interstitial position to another. The key factors which help drive diffusion are size of the interstitials, amount of vacancies, temperature and microstructure [44]. The size of the interstitial will determine how easily the atom can move through the lattice. The amount of vacancies allows for more atoms to move from lattice spot to lattice spot. Thus increasing the diffusion rate. Temperature has the greatest influence on diffusion. At different temperatures, diffusion coefficients can increase by orders of magnitude.. For example, for C diffusing into α-Fe, the diffusion coefficient increased from $2.4x10^{-12}$ to $1.7x10^{-10}$ cm^2 /s when the temperature increases from 500 ºC to 900 ºC. BCC and FCC crystalline structure affects diffusion of atoms. Iron has a BCC (α-Fe) and a FCC (γ-Fe) phase. [45] Carbon settles in octahedral sites in the FCC and BCC lattices. The size of the octahedral void in α-Fe (BCC) is 0.159R which is considerable smaller than γ-Fe (FCC) size of 0.414R. FCC structures have more sites for carbon to settle in. The solubility of

carbon in γ-Fe is about 2.15% compared to 0.03% in ferrite [44]. Figure 11 shows the diffusivity of different metal systems.

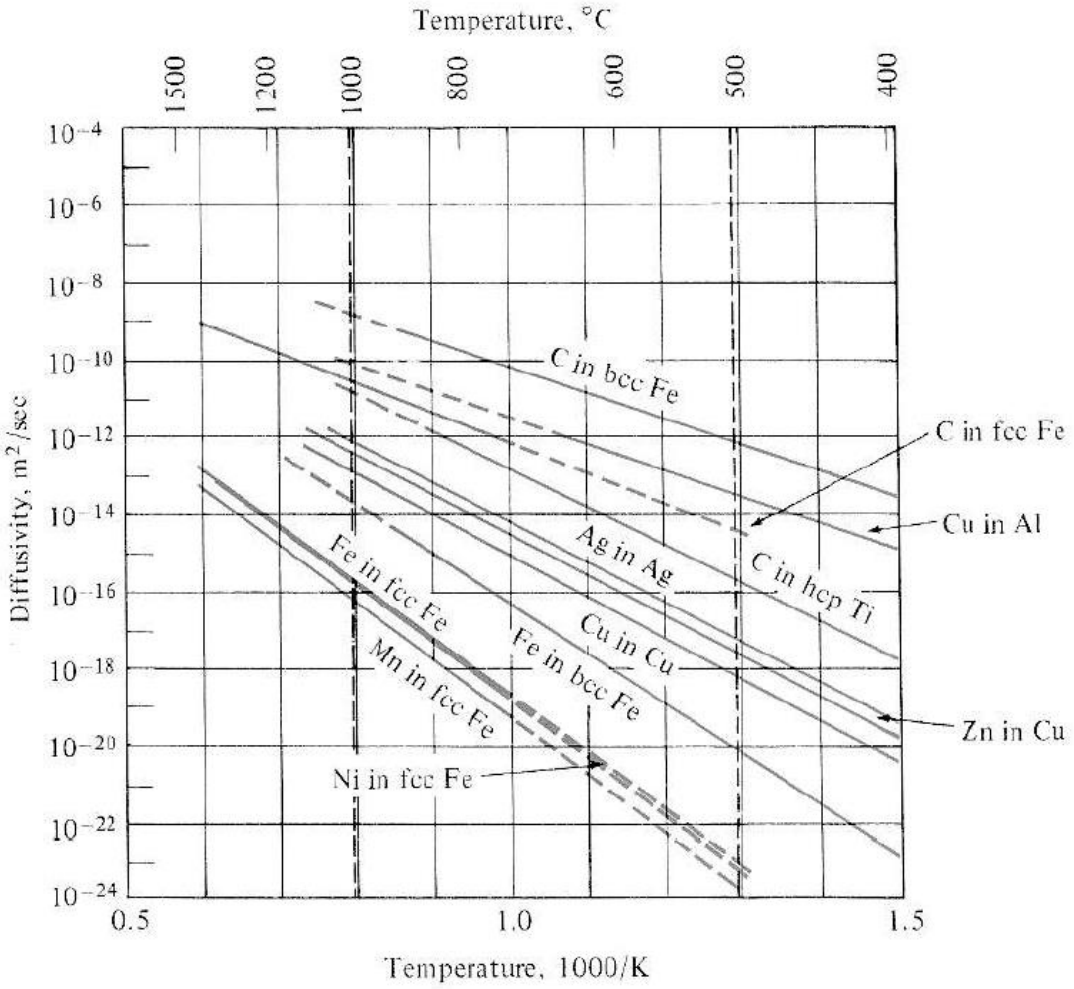

Figure 11. Arrhenius plot of diffusivity for different metal systems[45]

Ostwald ripening is a second phase coarsening, where small precipitates dissolve and redeposit into larger precipitates [43]. Ostwald described ripening in a two-phase system. The derived three equations to describe ripening, kinetic, continuity, and mass conservation equations. The kinetic equation describes growth and shrinkage rate of the precipitate. The continuity equation describes evolution of a particle size distribution. The mass conservation equation ensures that mass is not created or destroyed and must be

satisfied by the kinetic and continuity equation. Modification to Ostwald ripening includes the LSW theory [43]. LSW theory modified Ostwald ripening theory to a power-law growth and dynamic scaling. The theory also assumes precipitates and lattice are fluids and spherical under steady state condition.

The formation of precipitates typically requires very high temperatures and long annealing times. Figure 11 shows the time-temperature-transformation diagram (T-T-T) of the common precipitates in Alloy 718.The graph states γ" precipitates as Ni_3Cb.

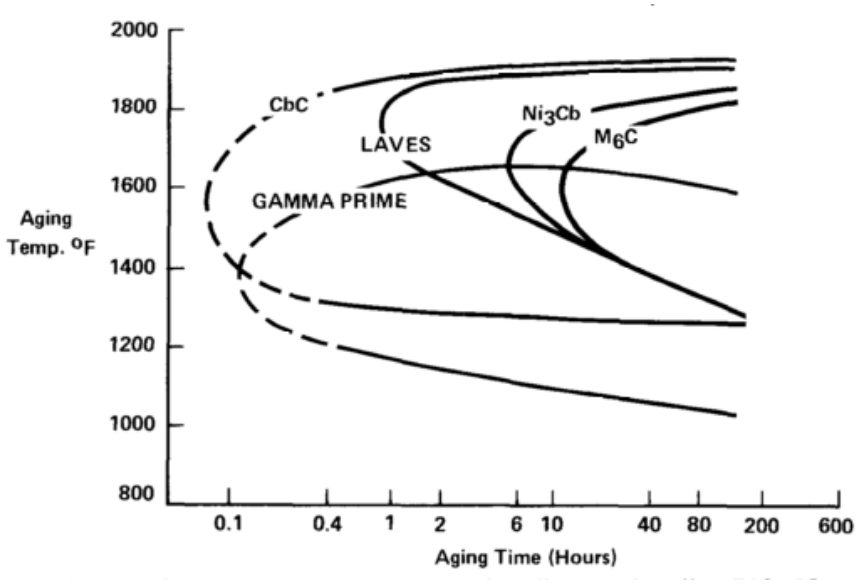

Figure 12. T-T-T for Alloy 718. The graph shows γ′ formation is favorable in intial annealing stages. [46].

Figure 9 indicates a driving force for precipitate formation is high temperatures and long annealing times.

The formation of precipitates can be aided by external forces. Applied stress to a material can cause defects and impurities to flow in the direction of stress. The impurities and defects can accumulate. The accumulation of impurities could lead to the formation of precipitates under stress conditions.

The formation of γ" precipitates under external and residual stress during thermal aging was study by H. Qin et al. [47]. The study tests different external stresses while keeping the same thermal aging process the same. The study concluded the nucleation and precipitation of γ" precipitates are strongly promoted by external stress in the early stages of aging. The volume fraction of γ" precipitates under external stress is initially higher than samples with no external stress during the first 0.5 hours of thermal aging but will gradually reach similar volume fractions with longer aging times. Precipitates formed under external stress tend to have smaller radius than samples with no external stress.

2.2.2 Formation of Precipitates during Irradiation

Under irradiation conditions, due to increased mobility of the atoms an increase can be observed in the number of point defects clusters. Radiation induced segregation (RIS) and radiation enhanced diffusion (RED) allow for greater mobility of atoms in the lattice. The mobility of atoms could lead to the enrichment and depletion of elements in the lattice. Thus, the process can destroy existing precipitates or create new precipitates in the material. Existing precipitates can display dissolution or disordering. Dissolution and disordering will be discussed later in this section. Precipitates have been observed to form under irradiation [22,48]. In a Ni-Si and Ni-Al system, precipitates have been observed to form at grain boundaries, surfaces and interior dislocation clusters [22]. Since Si and Al atoms are much smaller than Ni, the atoms have a higher mobility. The mobility of the smaller atoms finds sinks such as grain boundaries, surfaces and interior dislocation clusters and over saturates the areas. The over saturated sinks create an environment for the formation of precipitates. In Ni-Si and Ni-Al systems, γ' precipitates that have the

composition of Ni_3Al form. To the best of our knowledge, no studies have proven the formation of γ" precipitates under irradiations.

2.1.3.1 Dissolution and Disordering

Dissolution is the process of diffusion of precipitates back into the original lattice of the material under irradiation conditions. The damage done to the precipitate and the surrounding area creates an environment in which the atoms in the precipitates diffuse into the surround matrix. The dissolution of precipitates can be estimated by the following equations [22]. The Equation 4 describes the shrinkage rate of a precipitate.

$$\frac{dV}{dt} = -4\pi r_p^2 \zeta K_0 \Omega \qquad \text{Eqn. 4}$$

Where, r_p is radius of precipitate, ζK_0 is atoms leaving the precipitate per area per second and Ω is atomic volume.

The shrinkage term assumes the precipitate to be spherical which is known to be incorrect for γ" precipitates. The growth of the precipitate is defined as the following equation anddescribed by diffusion. Where D is the solute diffusion coefficient, C is the total concentration of solute, C_s is the concentration of solute in solution, C_p is the concentration of solute in the precipitate and ρ is the density of precipitates in solution.

$$\frac{dV}{dt} = \frac{3DC_s r_p}{C_p} \qquad \text{Eqn. 5}$$

The concertation of the precipitate is defined as,

$$C = \frac{4}{3}\pi r_p^2 \rho C_p + C_s \qquad \text{Eqn. 6}$$

Combining growth rate and shrinkage rate will yield overall growth rate of the precipitate which is define as,

$$\frac{dV}{dt} = -4\pi r_p^2 \zeta K_0 \Omega + \frac{3DCr_p}{C_p} - 4\pi r_p^4 \rho D C_p \quad \text{Eqn. 7}$$

If the equation is positive, then the precipitate is more favorable to grow.

Chemical mixing of precipitates and the matrix are caused by displacement cascades and thermal spikes. Klatt et al. describe the mixing parameter as a function of thermal spikes and displacement cascades as shown below [49]. Where k is the mixing parameter, D_m is intermixing diffusion coefficient, F_D is the damage energy deposited per unit length, Φ is ion fluence and t is the irradiation time.

$$k = \frac{D_m t}{\Phi F_D} = \left(\frac{\langle Dt \rangle}{\Phi F_D}\right)_{collision} + \left(\frac{\langle Dt \rangle}{\Phi F_D}\right)_{thermal\ spike} \quad \text{Eqn. 8}$$

Disordering can be described as the loss of long-range order to irradiation [22]. Disordering happens when the lattice structure is damaged by radiation but there is a small amount of diffusion. The disordering of a precipitates can be quantified by the electron beam spot electron of a TEM electron backscatter diffraction pattern. The disordering rate of a precipitate can be described using the model from Liou and Wilkes [22]. The disordering rate is determined by irradiation induced disordering and thermal reordering.

$$\left(\frac{dS}{dt}\right) = \left(\frac{dS}{dt}\right)_{irr} + \left(\frac{dS}{dt}\right)_{th} \quad \text{Eqn. 9}$$

Where $\left(\frac{dS}{dt}\right)_{irr}$ is define below and ε is disordering efficiency, K_0 is damage rate and S is long range order parameter.

$$\left(\frac{dS}{dt}\right)_{irr} = -\varepsilon K_0 S \quad \text{Eqn. 10}$$

Where $\left(\frac{dS}{dt}\right)_{th}$ is define below and S_e is the equilibrium order parameter and k_0 is the rate constant for ordering reaction.

$$\left(\frac{dS}{dt}\right)_{th} = \frac{k_0(1-S)^2}{(1-S_e)} - (1-S_e)K_0 \quad \text{Eqn. 11}$$

2.1.3.2 Coherent Nucleation

Coherent nucleation is the formation of a precipitate which continues the same lattice parameters of the surrounding matrix under irradiation conditions. The formation of a coherent precipitate is dominated by the vacancies in the material and the pseudo-free energy. The formation of precipitates can be described by the following equations. Where S_x is solute supersaturation, $B(X)$ is the fraction of solutes arriving at the precipitate, β_v is capture rate of voids, β_i is capture rate of interstitials, ρ_v is the number of clusters with trapped interstitials, ρ_i is the number of clusters with trapped vacancies and ρ_n is the number of clusters with no trapped defects. The total number of clusters is defined as $\rho_t = \rho_v + \rho_i + \rho_n$. The fraction of solutes arriving at the precipitate, $B(X)$, is calculated by the equation below.

$$B(x) = \frac{\beta_v(x)[\rho_v(x)+\rho_n(x)]+\beta_i(x)[\rho_i(x)+\rho_n(x)]}{[\beta_v(x)+\beta_i(x)]\,\rho_t(x)} \qquad \text{Eqn. 12}$$

The pseudo-free energy is calculated by the following equation,

$$\frac{\partial G'(x)}{\partial x} = -kT \ln S_x + kT \ln B(X) \qquad \text{Eqn. 13}$$

Plotting each term separately can determine the number of roots, 0, 1, or 2, the terms may have in common. The solid solution is considered stable if there are zero roots. With one root, the solution is considered a metastable state. In the case of 2 roots the solution is metastable below the value X, and the precipitate cannot grow to larger size.

2.2.3 Thermal and External Stress

Stress has been shown to assist the formation of γ" precipitates during the aging process. Two types of stress are exerted on the window, thermal and external. Thermal stress is caused by the expansion, due to temperature increase, by a temperature gradient across a material. The external stress comes from the window being under vacuum on one side and atmospheric pressure on the other side. To calculate stress due to thermal expansion, the following equations are used.

$$E = \frac{\sigma}{\epsilon} \qquad \text{Eqn. 14}$$

$$\epsilon = \frac{\Delta l}{l} \qquad \text{Eqn. 15}$$

$$\Delta l = \alpha \, \Delta T \, l \qquad \text{Eqn. 16}$$

Where E is elastic modulus, σ is stress, ϵ is strain, α is thermal expansion coefficient, ΔT is the temperature difference, l is the length of the material and Δl is the change in length of the material.

After rearranging and substituting last three equations, the stress can be calculating with the equation below.

$$\sigma = E \, \alpha \, \Delta T \qquad \text{Eqn. 17}$$

External forces cause deformation to the molecular structure of the material. A material can undergo external force from a difference in pressure. A rough estimate of external forces can be calculated by the difference of pressures multiplied by the area. As Shown in Eqn. 18.

$$F_{net} = \frac{P_a - P_v}{A}$$ Eqn. 18

Equation 18 does not consider material properties like the program Solidworks.

2.2.3.1 Solidworks

Stress analysis on the ion beam window was conducted using the finite elements analysis tool in Solidworks. The Solidworks model chosen was the linear elastic isotropic model. The model assumes that the material does not change material properties in any direction. The model also assumes young's modulus follows a linear relationship.

2.3 Ion Depth and Energy Deposited Simulations

2.3.1 Stopping Range in Matter (SRIM)

SRIM is a Monte Carlo code which stands for the stopping and range of ions in matter[50]. The core of the program SRIM is TRIM, which is Transport of Ions in Materials. SRIM's main goal was to establish a program to model the stopping and range of ions while using unified theoretical concepts [50]. TRIM can be used to calculate the vacancies created by projectile, cascades, ion ranges in 3-Dimensions, energy loss due to ionization, energy loss due to phonons and energy loss due to displacement in a given material. TRIM can also be used to estimate the dpa in a material for heavy and light ions.

SRIM uses two approximations, analytical formula for determining atom to atom collisions and Free-Flight-Path between collisions. The atom to atom collisions theory used in SRIM, is referred to as the Magic formula in the SRIM handbook [50]. The Magic formula technique was developed by Biersack and co-workers for faster computational time [51]. The Magic formula allowed for a quick and precise solution to obtain a scattering angle. The scattering angle is then used to calculate the energy loss due to atom to atom

collisions. SRIM is a Monte Carlo code which uses random numbers to generate the probability of a scattering angle. The energy loss per collision is given by the energy loss equation shown below. Where T is the amount of energy loss, M_1 is the projectile mass, M_2 is the target mass, E is the projectile energy and φ is the scattering angle.

$$T = \frac{4M_1M_2}{(M_1+M_2)} E sin^2\left(\frac{\varphi}{2}\right) \qquad \text{Eqn. 19}$$

The Free-Flight-Path approximation is used for a projectile between collisions. The approximation is only viable for charge particles. To obtain the free path length of a projectile the following equation is used. The parameters of Eqn. 17 below will change depending on the size and energy of the projectile. If the particle is relativistic than the ε parameter will change.

$$L = \frac{0.02\,[1+(M_1+M_2)]^2}{4\pi a^2 N} \frac{\varepsilon^2+0.1\varepsilon^{1.38}}{\ln(1+\varepsilon)} \qquad \text{Eqn. 20}$$

Where L is path length, N is electron density and ε is consider the reduce energy.

SRIM follows a computational algorithm. SRIM first starts with the known energy of the projectile, E. The code randomly picks an impact parameter. The impact parameter is perpendicular distance between the projectile path and the center of the target. Then it uses the Magic Formula to calculate the new scattering angle. With the new scattering angle, the energy transfer to the atom is calculated. For detailed cascades calculations, the energy transfer to the atom is the kinetic energy of the atom minus the displacement energy until the energy of the atom is smaller than the displacement energy of the material. The free-flight-path is calculated. The projectile is followed until the ion energy is too low to

create a displace atom. SRIM repeats this process, while making tallies of important numbers, until statistics are good.

SRIM can be used to calculate the dpa in a material. To calculate the dpa the following recommendations by Stoller et al. [52] are to use the "Quick" Kinchin and Pease option, for iron base alloys use 40 eV for the displacement energy and set the binding and lattice energies to 0 eV. Once the SRIM calculation is complete then the vacancy output file is used. The output file will obtain a number of vacancies/ion-Angstrom and the calculated atomic number density. The ion flux is from the experiment being conducted. The equation to calculate dpa is shown below.

$$\frac{dpa}{s} = [ion\ flux] * [SRIM\ OUTPUT] * [atomic\ density] \quad \text{Eqn. 21}$$

The total dpa can be calculated by multiplying the exposure time with the dose rate.

The disadvantage of using SRIM is at relativistic energies with light ions, the program does not make the correct assumptions. SRIM will under estimate the damage and energy deposited. SRIM does not take into account the crystal lattice, nuclear reactions and damage accumulation.

2.4 Literature Review and Notable Work

Inconel 718 has been tested under a variety of irradiation and temperature conditions. These sections will talk about previous experiments of Inconel 718.

2.4.1 Ion Beam window at LANSCE Facility

During preventative maintenance at the LANSCE facility at LANL, the ion beam window was replaced and studied [31]. The ion beam window was in operation for about 5 and half years and was subjected to 100 MeV, 250 μA beam, thermal heating by irradiation and stress induced by a differential pressure across the beam window. The ion beam window was made of solution annealed Inconel 718. Therefore, γ' and γ'' precipitates are not expected to be in the matrix of the material. The thermal analysis of the ion beam window estimated the maximum temperature to be around 122 ºC. MCNPX heating tallies, computational fluid dynamic code ANSYS CFX and ANSYS finite-element where used to

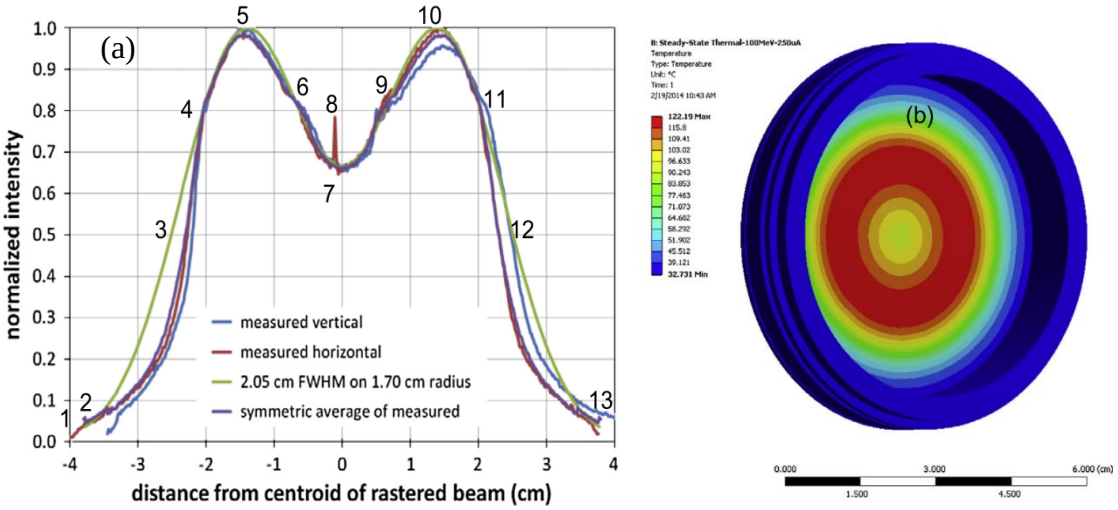

Figure 13 Temperature profile of the ion beam window [31]

estimate a steady-state temperature profile. The temperature and dose profiles of the ion beam window exhibit an annular shape as in Figure 10 below.

The maximum dose was estimated to be around 11.3 dpa. The high dose irradiation area was located closer to the edge of the ion beam window. The dose at the outer edge of the ion beam window was estimated to be about 1 dpa. Shear tests and microstructural analysis

was investigated in all regions of the ion beam window. At the areas of about 11.3 dose, radiation induced defects harden the material according to shear punch tests. TEM analysis indicated no change in microstructure no voids were observed. Analysis of the outer edges had more interesting results with respect to microstructure changes than the other areas of the ion beam window. Shear punch testing indicated a significant increase in hardening

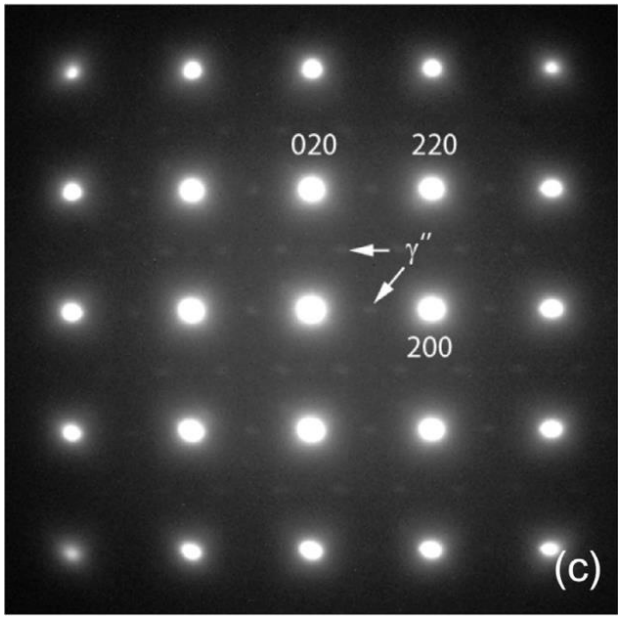

Figure 14 TEM diffraction pattern of γ″ precipitates [31]

compare to inner ion beam window specimens. TEM analysis showed the increase in hardness was contributed to the formation of γ" precipitates in selected area diffraction patterns. The TEM diffraction patterns are shown below in Figure 11.

The formation of γ" precipitates was unprecedented. The γ' and γ" precipitates are known to be disorder and have dissolution occurred. The next section will talk about these studies.

2.4.2 Previous Studies of Inconel 718 Under Irradiation Conditions

The tensile properties of both SA and PH Inconel 718 was investigated after low temperature neutron irradiation by Byun et al [36]. The experiments tested multiple

samples of SA and PH at an estimated dose range of 0.00057 to 1.2 dpa. The samples kept to an estimated temperature range of 60-100 ºC and at a fluence range of 3.7 x 10^{21} to 7.8 x 10 ^{24} nm^{-2} of a fast neutron spectrum (E > 1 MeV). After irradiation, the samples underwent tensile tests at room temperature. PH Inconel 718 exhibit minor radiation-induced increase in yield strength and a significant decrease in ductility. SA Inconel 718 had almost three times increase in yield strength from the unirradiated sample to 1.2 dpa sample. No microstructure analysis was performed with these tests.

In 1996, a crack in the LANSCE facility double shell proton beam window was noticed. The ion beam window was exposed to 1 mA, 800 MeV protons beam. The highest amount of dose to the beam window was estimated to be about 20 dpa. Tensile and hardness experiments were done by James et al. [39]. The Inconel 718 window was cut into samples based on estimated dose for tensile testing. The samples in regions which were irradiated to 20 dpa, had a higher yield strength (YS) and broke in the elastic regime compared to the non-irradiated samples which show significant elongation. The study compared and concluded the increase in YS to be similar to reactor neutron irradiation data on Inconel 718 [39]. Hardness tests indicated radiation induce softening of PH Alloy 718, for regions of 5-20 dpa of the beam window.

Precipitated hardened Inconel 718 was investigated under in situ Ar ion irradiation at the Accelerator Laboratory of Wuhan University in China by Jin et al. [35]. The test was conducted at elevated temperatures of 290 and 550 ºC and at a current of 0.8-1 μA/cm^2. The dose reached about 30 dpa for the experiments at 550 ºC and about 5 and 15 dpa at 290 ºC. The selected-area electron diffraction (SAED) patterns was taken in the [110] zone axis direction as shown in Figure 12.

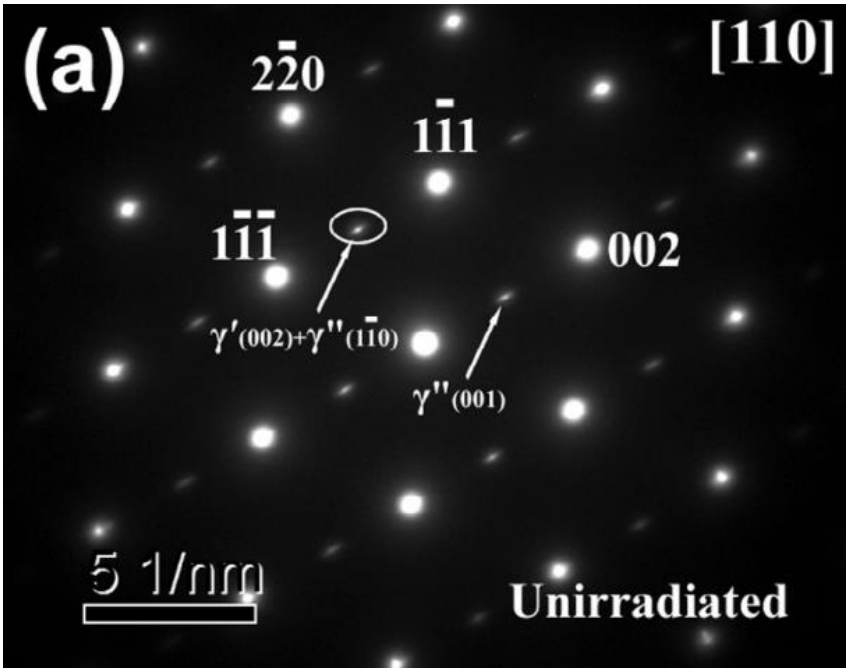

Figure 15. SAED of γ' and γ'' in the [110] zone axis [35]

Disordering of the precipitate was discovered at 5 dpa at a temperature of 290 ºC. The γ'' precipitate order was completely destroyed by Ar ion irradiation at both temperatures. The observed size of γ' and γ'' precipitate gradually decreased from about 23 nm to 14 nm.

The Spallation Neutron Source (SNS) group, at Oak Ridge National Laboratory conducted microstructure analysis of Inconel 718 as a possible candidate material for the accelerator beam window [40,53]. The experiments tested both PH and SA Inconel 718 with 3.5 MeV Fe^+, 370 keV He^+, and 160 keV H^+ either singular or simultaneous. Fe^+ and $Fe^+ + He^+ + H^+$ ion irradiations reached a dose of about 10 dpa. At 0.1 dpa, SA Inconel 718 microstructure exhibit Frank type faulted loops. As the dose increase, faulted loops turn into perfect loops and cavities were observed. The experiment did not publish any electron diffraction patterns of SA Inconel 718 and found no evidence of precipitate formation. SA Inconel 718 showed radiation induced hardening while PH Inconel 718 exhibit radiation induced softening [40]. The test concluded that hardening in SA Inconel 718 is due to

radiation induce defects. PH Inconel 718 showed signs of disordering of γ' and γ" precipitates around 0.1 dpa Fe^+ and 0.2 at. % He^+ irradiation [53]. The γ' and γ" precipitate diffraction pattern completely disappeared at 1 dpa Fe^+ and 2 at. % He^+.

The effects of neutron irradiation on PH In718 was investigated by Thomas and Bruemmer [29]. The experiment investigated microstructure and grain boundary compositions in PH Inconel 718 at 288 ºC. The temperature was chosen to replicate the temperature found in most PWRs. During microstructure investigation of the as received materials, γ" precipitates were noted to be forming at the grain boundary. The formation of γ" precipitates was contributed to the higher concentration of Nb at the grain boundaries. After an estimated dose of 2.5-3.5 dpa γ" precipitates disorder completely and γ' precipitates still had a presence in the diffraction pattern. At 20 dpa, both γ' and γ" precipitates completely disordered. For all doses Frankel dislocation loops were discovered and ranged in size from 10 nm to 40 nm. At 20 dpa, cavities were observed in the sample. The initial grain boundary composition about 8% Nb and 4% Mo. During neutron irradiation, Nb and Mo concentrations reduced in the grain boundaries while Cr and Fe increased with the increase of dose. The hardness test on the irradiated material showed about a 30% decrease from the unirradiated sample to the 20 dpa sample.

Sundararaman et al. studied the stability of γ' and γ" precipitates under electron irradiation [54]. Electron irradiation can create displacements of atoms but not the damage cascades seen in ion and neutron irradiations. The PH Inconel 718 samples were irradiated with electrons at the ultra-high voltage electron microscope at Osaka University. The fluence of the electron beam was about 1.15×10^{24} electrons/s/m^2 at an energy of 3 MeV. The corresponding dose rate was calculated to be about 10^{-3} dpa/s according to

Sundararaman et al. The time irradiated for each same was 15 minutes. The temperatures at which irradiation occurred were room temperature, 400 ºC, 500 ºC and 650 ºC. The average size of γ" precipitates was measured to be about 19 nm. Diffraction patterns were taken in the [001] zone axis. At room temperature, disordering was observed but the γ" precipitates did not completely disorder. At 400 ºC and 500 ºC disordering was observed with a much weaker diffraction pattern for γ" precipitates than at room temperature. At 650 ºC the γ" precipitates diffraction pattern was enhanced. The temperature was about 0.5 of the melting temperature of Inconel 718. The thermal diffusion of atoms is much higher at elevated temperatures and Sundararaman et al concluded this was much greater than the destruction of precipitates.

The Accelerator Production of Tritium (APT) project investigated candidate materials, 316L/304L stainless steels, PH Alloy 718 and Mod 9Cr-1Mo, under spallation environments conditions [13]. The spallation environment is 1 GeV proton beam which is shot at a tungsten target to induce a (p,n) reaction. The environment produces high energy neutrons along with non-absorbed high energy protons. The tensile strength and fracture properties of the candidate materials were studied. The test studied PH Alloy 718 from 0.5 dpa up to 10.8 dpa. For a dose of 0.5 and 2 dpa, the study found a slight increase in YS while fracture toughness and uniform elongation declined. It was also shown that the YS at higher doses decreased about 20% from 2 dpa to 10.8 dpa. The decreases are contributed to the disordering of the irradiation sensitive precipitates.

The investigation on Inconel 718 irradiated with 800 MeV protons investigated microhardness, bend strength tests and microstructure [55]. The PH Inconel 718 samples were used as a neutrino source at the Los Alamos Meson Physics Facility (LAMPF) which

is currently called LANSCE. The shape of Inconel 718 samples were two concentric spheres. The highest dose rate calculated was 10 dpa. A decrease of about 20% hardness was observed as dose increased to 10 dpa. The hardness was calculated as a function of radial position. At the center the hardness was observed to be the lowest with the edges of the sphere showing an increase in hardness. The softening of the material could be explained by the dissolution of γ' and γ'' precipitates at were the higher doses occurred. The hardening of PH Alloy 718 was not explained, and the phenomena not seen in any other technical documents. TEM analysis showed diffraction patterns of the super lattice, γ' and γ'' precipitates not fully disappearing at 10 dpa.

A study by Sencer et al. investigated the mechanical properties and microstructural development of PH Alloy 718 irradiated with mixed spectra of high-energy protons and spallation neutrons [27,30]. The specimens were irradiated at the LANSCE accelerator at 800 MeV 1mA protons and placed in low exposure in neutron furnaces. The experiment was to simulate the APT environment of a spallation environment of 1 GeV protons. The samples had a range of doses and temperatures that depends on the position and the beam intensity. At 0.1 dpa the temperature was about 72 ºC and at 0.6 and 13.4 dpa was about 32-55 ºC, respectively. Disordering was noticed at 0.1 dpa but the superlattice reflection was still faintly visible. At 0.6 dpa the superlattice reflection was completely gone [30]. The precipitate solutes did not fully redistribute back into the matrix. Thus, retaining some of the strength of the material.

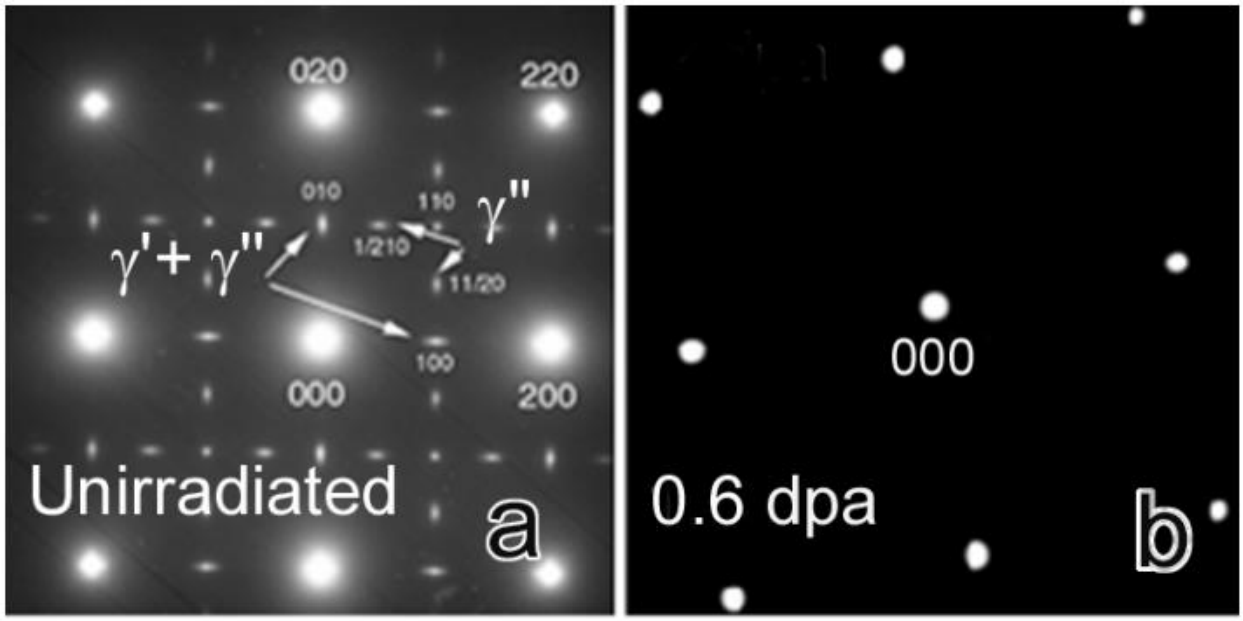

Figure 16 Disordering of γ'' precipitates after 0.6 dpa of dose [30]

2.4.3 Notable Nickel-Base Alloys Under Irradiation Conditions

Rene N4 is a nickel base super alloy being considered for similar applications as Inconel 718 and Nimonic PE 16. Rene N4 forms much larger, about 450 nm in diameter, γ' precipitates than both Inconel 718 and Nimonic PE 16 which are around 20 – 30 nm in diameter. Sun et al [56] investigated the disordering and dissolution of γ' precipitates in Rene N4. The test was conducted with *in situ* and *ex situ* ion irradiations. Kr^{2+} and Ni^{3+} ions with energies of 1 MeV and 3 MeV were the choice of ions for *in situ* ion irradiation. The tests were conducted at Argonne National Laboratory IVEM and Sandia National Laboratory I^3TEM. The *in situ* ion irradiation went up to 0.3 dpa and found immediate disordering of γ' precipitates. *Ex situ* experiments with Ni^{3+} ions with an energy of 3 MeV was conducted at the Ion Beam Materials Laboratory in Los Alamos National Laboratory using a Tandem accelerator. The *ex situ* went up to a dose of 75 dpa. The results concluded

large γ' precipitates were still visible, although partially dissolved into the surrounding solution.

Zhang et al. has investigated Inconel X-750 under both neutron and ion irradiations [34,57]. Inconel X-750 is used in CANDU reactors for fuel channel spacers and as cable sheathing. Inconel X-750 has a higher concertation of aluminum compared to Alloy 718 and Nimonic PE16. The investigation of neutron irradiated sample showed irradiation(?) induced instability of γ' precipitates. The superlattice spots decrease in intensity which proved some disordering [57]. When Inconel X-750 was investigated under Kr^{+} irradiation, disordering and dissolution was observed [34]. The material was investigated across a range of temperatures and doses as shown in the Figure 17.

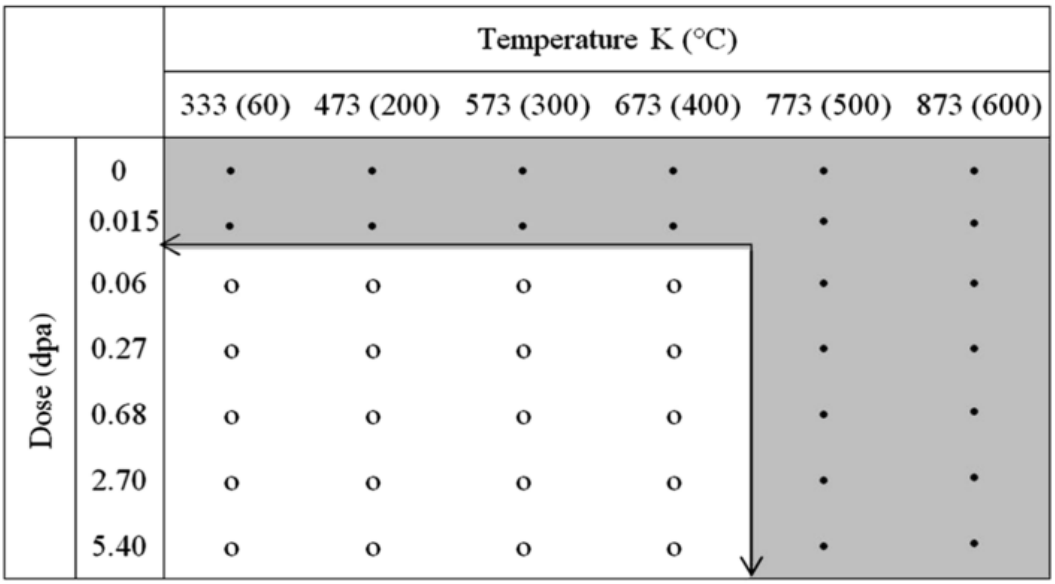

Figure 17. ○idicates disordering ● indicates no disordoring [34]

The γ' precipitates reached a critical temperature of 500 ºC which the precipitates do not disorder after irradiation [34]. The γ' precipitates irradiated at temperatures under 500 ºC did exhibit disordering. EDX mapping shows dissolution of the γ' precipitates at 5.4 dpa [34].

Nimonic PE 16 is a nickel bas alloy similar to Alloy 718. Nimonic PE16 has more aluminum in solution than Alloy 718. With the increase of aluminum, more γ' precipitates are present in the material. Bourdeau et al. investigated the disordering and dissolution of γ' precipitates under ion irradiation [33]. The stability of γ' precipitates was investigated under 300 keV Ni^+ ion irradiation at room temperature. The dose varied from 0.001 dpa to 2 dpa. To determine the kinetics of disordering, the intensity of the superlattice reflections was compared to non-irradiated specimens. Disordering of the γ' precipitates occurred between 0.1 and 1 dpa. Bourdeau et al. claimed after 2 dpa the vanishing of the superlattice spots is caused by the dissolution of the γ' precipitates.

Chapter 3: Materials and Methodology

3.1 Solution Annealed Inconel 718

Alloy 718 is a high-strength and corrosion resistant nickel base alloy. The alloy is produced in two different forms: precipitation hardened (also referred as annealed and aged) and solution annealed. Precipitation hardened Alloy 718 has two precipitates γ' and γ" which attribute to the strength of the material. Alloy 718 is a readily fabricated alloy with exceptional tensile, creep, rupture, and fatigue strength [24]. The ease and economical fabrication of Alloy 718 allows the alloy to be use in a wide variety of applications [13,36,40,59]. The physical properties of both forms of Alloy 718 are shown in Table I below.

Table 2. Important Physical Properties of Non-Irradiated Alloy 718 [24]

Density	
Annealed	0.296 $\frac{lb_m}{in^3}$ (8.19 $\frac{g}{cm^3}$)
Annealed and aged	0.297 $\frac{lb_m}{in^3}$ (8.22 $\frac{g}{cm^3}$)
Melting Range	2300 – 2437 ºF (1260-1336 ºC)
Poisson Ratio at 70 °F, (at 21°C)	0.29
Specific Heat at 70 °F, (at 21°C)	0.104 Btu/lb °F (435 J/kg °C)
Thermal conductivity at 70 °F, (at 21°C)	77 BTU•in/ft2•h•°F (11.1 W/m-ºC)

Alloy 718 consist mainly of Ni, Cr, and Fe but include small amounts of Molybdenum, Niobium, Tantalum, Titanium and Aluminum. High Cr contents in the alloy gives excellent oxidation resistance. Titanium, aluminum and niobium contribute to the strength of Alloy 718 by forming γ' (Ni_3(Al,Ti)) and γ" (Ni3Nb) precipitates. Molybdenum aids in high temperature stability and strength [59]. Columbium is another term for niobium and tantalum and is used in older references [60]. Table II shows the composition range of Alloy 718 and the maximum amount of impurities the alloy can have.

Table 3. Composition Range of Alloy 718 (wt%)[24,60]

Nickel	50.00-55.00
Chromium	17.00-21.00
Iron	Balance
Columbium (Nb+Ta)	4.75-5.50
Molybdenum	2.80-3.30
Cobalt	1.00 Max.
Aluminum	0.20-0.80
Titanium	0.65-1.15
Manganese	0.35 Max.
Silicon	0.35 Max.
Boron	0.006 Max.
Carbon	0.08 Max.
Sulphur	0.15 Max.
Phosphorus	0.015 Max.
Copper	0.30 Max.

3.1.1 Annealing Processes

Annealing is the process of heating a metal to a very high temperature to allow atomic diffusion to occur [45]. The process allows for a material to increase in ductility and reduce internal stresses and dislocation density that could contribute to brittleness. After heating up the material, precipitation hardening is the next step. Precipitation hardening is the hardening and strengthening of the material by the dispersion of particles that precipitate from the super saturated solid solution [44]. According to Special Metals Corporation, there are two ways Alloy 718 are heat treated and sold. Both ways start off with solution annealed Alloy 718. The first heat treatment process heats the material to a temperature of 1700-1850 ºF (925-1010 ºC) followed by rapid cooling in water. The material then undergoes precipitation hardening at 1325 ºF (718 ºC) for 8 hours. The next

step is thermally ageing the material at 1150 ºF (620 ºC) for 18 hours and then air cooled. The second treatment for PH Alloy 718 process heats the material to 1900-1950 °F (1038-1066 °C) followed by rapid cooling, usually in water. After the rapid cooling the material is thermal aged to induced precipitate growth. The material is held at a constant temperature of 1400°F (760 °C) for 10 hours then furnace cool to 1200°F (649 °C). The final step in the annealing process is holding the Alloy 718 at 1200 °F (649 °C) for a total aging time of 20 hours and finish with air cooling. The two heat treatments are recommended for different application at room temperatures. Special Metals Corporation recommends higher temperature annealed Alloy 718 be used in tensile-limited applications.

3.1.1 Mechanical Properties

The mechanical properties of Alloy 718 are very promising compared to other Ni base alloys and metals commercially available. Tensile strength, modulus of elasticity, hardness, elongation and fatigue are among the most commonly used properties to explain

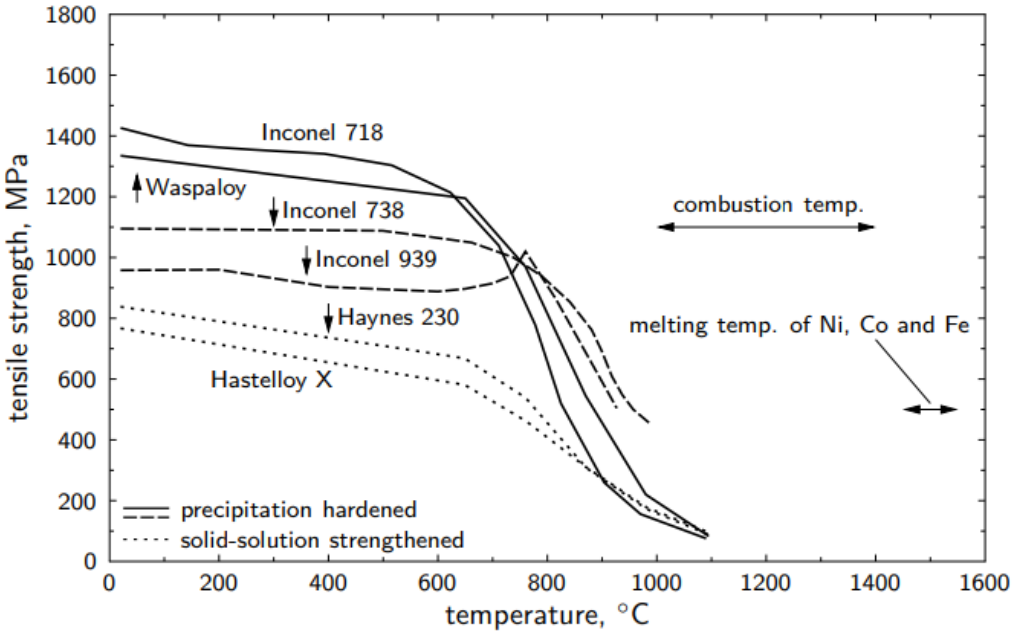

Figure 18 Tensile strength of various nickel base alloys as a function of temperature [73]

the durability and strength of a material. Figure 18 illustrates the tensile strength of selected nickel base alloys as a function of temperature. Tensile strength is the capability of a material to withstand a tension or pulling force [44] Alloy 718 has great tensile strength, compared to other nickel base alloys, at temperatures below 650 °C. The alloy has similar tensile strength as Haynes 230 and Hastelloy X at higher temperatures. The figure illustrates the tensile strength of selected nickel base alloys as a function of temperature.

The hardness of a material is the resistance to deform surface indentations or abrasions. Hardness and how it is calculated will be discuses in greater detail further on in Section 3.1.2. Alloy 718 has higher hardness compared to other nickel base alloys such as

Waspaloy. Polvorosa et al. studied tool wear on bolts made of Alloy 718 and Waspaloy found that the hardness of Alloy 718 is greater than Waspaloy [58].

3.1.2 Nanoindentation

Nanoindentation is the process of testing for mechanical properties of materials with small volumes. Nanoindentation uses a small tip, ranging in different areas of contact, shapes, and materials types, to apply a load. The displacement of the tip and the load applied to the material can be used to determine hardness and Young's modulus. Figure 19

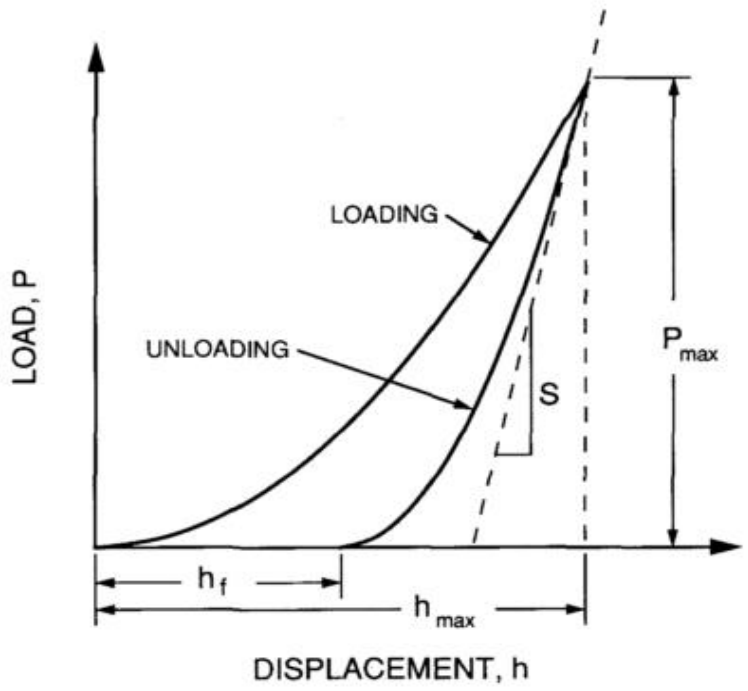

Figure 19. Nanoindentation loading and unloading curve. For the loading and unloading curve material properties can be calculated [9].

is the type of plot you would expect from a typical nanoindentation experiment. The displacement is plotted versus applied load during the nanoindentation test.

The plot shows two curves, loading and unloading curve. The slope of the unloading curve is used to calculate the stiffness, S, as shown in equation X. The reduced

Young's modulus, E_r can be solved for using equation X, with the known projected (also called indentation) area, A.

$$S = \frac{dP}{dh} = \frac{2}{\sqrt{\pi}} E_r \sqrt{A} \qquad \text{Eqn. 20}$$

The Young's modulus can be determined through equation X1, where E and ν are Young's modulus and Poisson's ratio for the specimen and E_i and ν_i are the same parameters for the indenter [61].

$$\frac{1}{E_r} = \frac{(1-\nu^2)}{E} + \frac{(1-\nu_i^2)}{E_i} \qquad \text{Eqn. 21}$$

The applied load is used to calculate the hardness, P_{load}, as shown in equation 20 below.

$$H = \frac{P_{load}}{A} \qquad \text{Eqn. 22}$$

Nanoindentation experiments were conducted at University of New Mexico (UNM) Extreme Materials Lab, using NanoMechanics iMicro nanoindenter. The nanoindenter setting was set to a max load of 1000 mN. Testing setup included 16 indents into the sample. The test had no depth limit and with a distance of 100 μm between the indents. The distance was chosen to insure the indents will not interact with one another. The load hold time was set to 0 seconds. The results were an average hardness of 3.99 ± 0.20 GPa and a Modulus of 221.6 ± 5.1 GPa. One indent was omitted because it did not extract any data from the indent.

3.1.3 FIB Imaging

The as received material shown in Figure 17 has an average grain size of 9.8 µm with many twins forming. The average grain size was calculated using the line intercept method. The image was taken using a Focus Ion Beam (FIB) at UNM. The FIB use Ga ions to image the Alloy 718 sample. Twins form under uniform stress across the lattice. The formation of twins occurs when the material is formed. A typical stacking pattern follows a pattern of ABCABC. In a twin the stacking pattern is mirrored, ABCCBA.

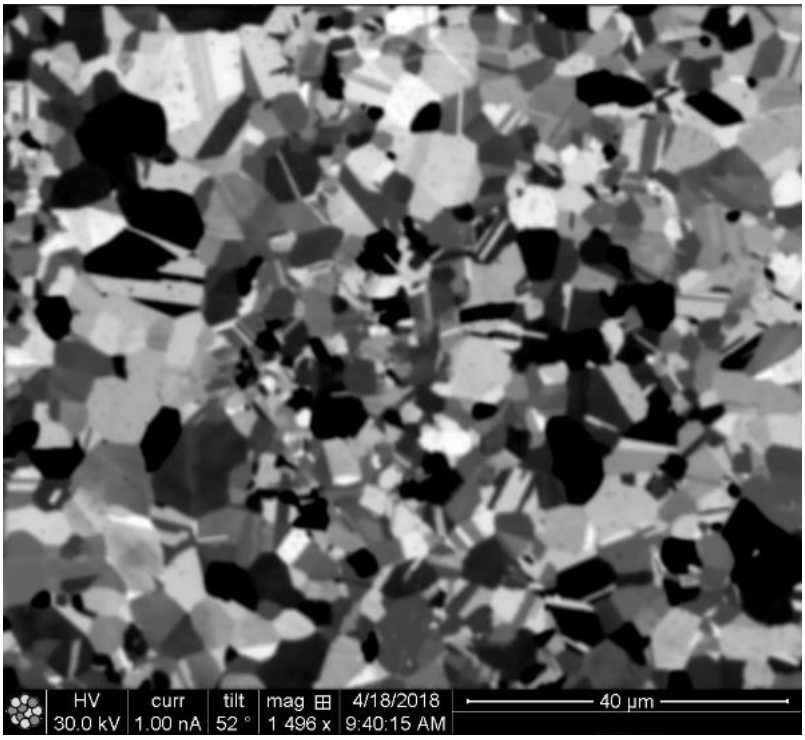

Figure 20. Grains in the received material of alloy 718 using the focus ion beam.

3.2 Sample Preparation

Bulk sample bars of Alloy 718 were obtained from LANL. Using a Buehler Ecomet 4 polisher/grinder, the material was ground and polished. The majority of the sample bars were thinned down to approximately 200 µm using 400, 600, 1200 and 2400 grit paper. The polishing of the samples used 1, 0.3 and 0.04 µm Silica slurry. For the *in situ* tests, the

samples were punched into 3mm disks. The samples were further thinned to electron transparency by twin jet electro-polishing at LANL.

Twin jet electropolishing is the process of thinning a sample by an electrochemical action. A 3mm sample is placed in a holder. The holder is placed into solution twin jet polisher. The solution used at LANL was 95% methanol and 5% perchloric. The solution and system are cooled by liquid nitrogen. The solution was kept at a temperature of around -35 ºC ± 5ºC. The holder is positioned between two jet nozzles and a light source with a photodetector. The photodetector determines the amount of light coming though the sample. The amount of light signifies the amount of material etched away. The samples were etched away to a reading of 30% light by the photodetector. The sample in the holder acts as an anode and the jets act as cathodes. The jet pump was set to the setting of 33 (no units were given). The voltage current behavior is very important to obtain a good sample. High voltage applied to the system can cause the material to pit/relief due to oxygen formation. Low voltage can exhibit etching effects due to direct anodic dissolution [62]. The voltage was maintained at 22V throughout electropolishing. The samples were inspected under an optical microscope.

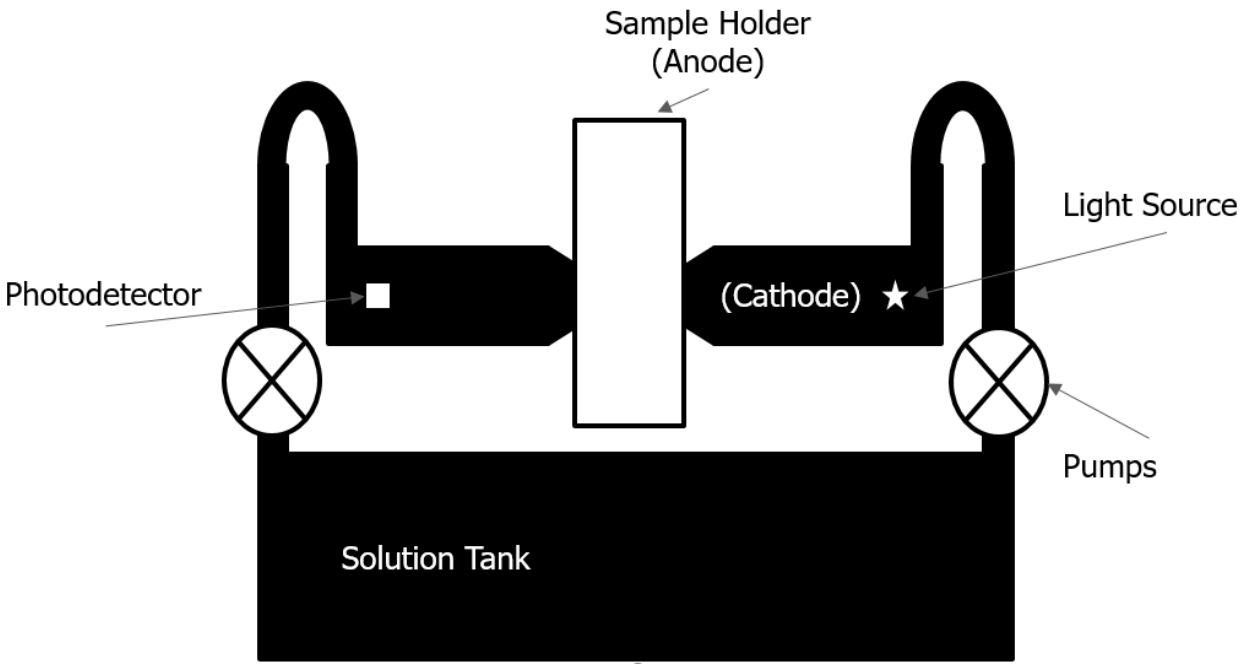

Figure 21. Twin jet electro polisher diagram.

3.3 In Situ Ion Irradiated Transmission Electron Microscopy Beam

3.3.1 Transmission Electron Microscopy (TEM)

TEM uses a beam of electrons to transmit through a specimen to emit an image. High energy electrons have a wave length shorter than high energy photons. The short wave length allows for a high resolution image. Most metallic specimens must be thinner than 100 nm to get a good TEM image. The high-resolution image is credited to the understanding of the de Broglie wavelength. The electrons can pass through the thin region, interact with the material and be detected to create an image. Figure 4 illustrates the basics of a TEM.

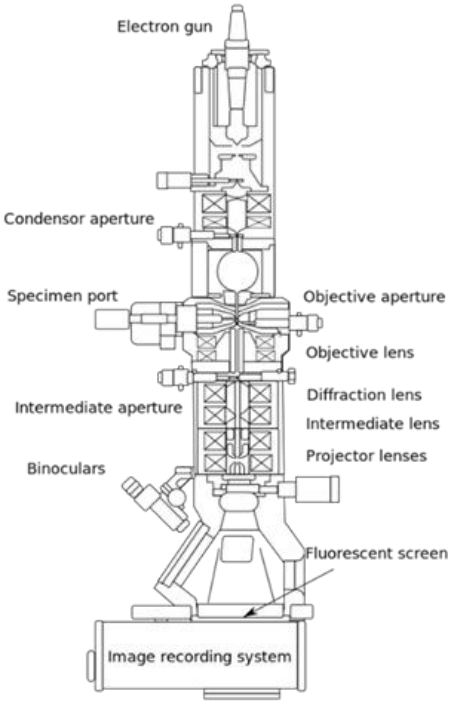

Figure 22. Schematic of TEM [63].

The electron gun, typically made out of lanthanum hexaboride, is the electron source. Other electron source includes tungsten, Shottky ZrO/W, Thermal FE W (100) and Cold FE W (310) [63]. The most commonly use are tungsten and LaB_6 because of low operational cost and easy maintenance [63]. The beam is then subjected to apertures and

magnets to focus the beam to desired location and size. Changing the apertures and condenser allows for different function on the TEM. The functions of TEM include Bright Field imaging, Dark Field imaging, and Electron Diffraction Pattern.

Electron Diffraction Patterns can be used to determine the crystal structure and orientation of the grains of the material being analyzed. By selecting the correct setting, apertures and a beam intensity a selected area diffraction pattern (SADP) image is created using a TEM. In a SADP, each diffraction spot corresponds to the electron beam scatter intensities. A zone axis of [001] will have a different SADP than the same material oriented

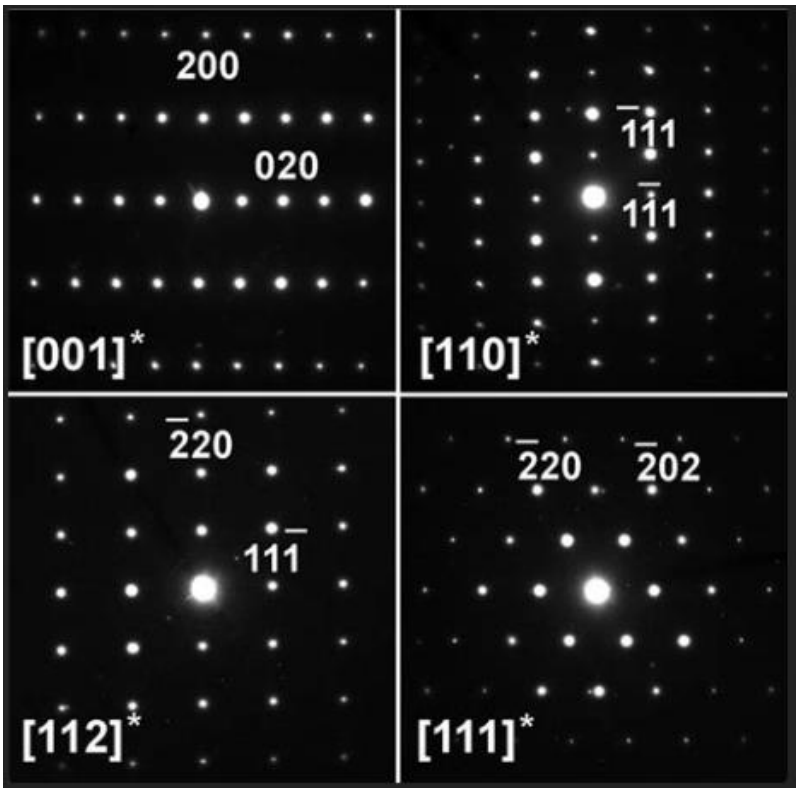

Figure 23. SADP in a FCC material at a different orientation [65].

along a zone axis of [013].

Changing the orientation of the specimen will lead to different diffraction conditions. A way of finding the zone axis is using Kikuchi lines [63,64]. Kikuchi lines are a pair of bands of electron diffraction from a single crystal structure [64].

Kikuchi lines form by diffusely scatters electrons in diffraction patterns. Kikuchi lines act

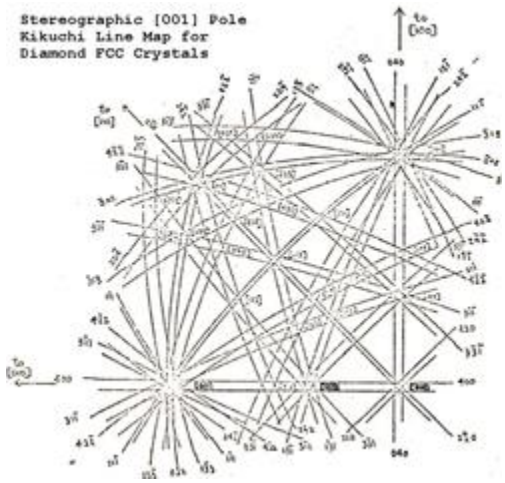

Figure 24. Kikuchi Line map for a FCC crystal

like a road map to lead one to different zone axes of the single crystal or grain in a material. FCC and BCC materials exhibit different SADPs and Kikuchi lines for different zone axis because of their different crystal structures [63,64].

3.3.2 Ion beams

Ion beams are comprised of many types of ions ranging from H+ up to U Ions that are accelerated using electrostatic and electrodynamic accelerators. Electrostatic accelerators use static magnetic fields to accelerate ions [65]. Examples of electrostatic accelerators are van Der Graaff and Cockcroft-Walton generators. Electrodynamic fields used magnetic induction or oscillating radio frequency to accelerate ions [65]. Examples of electrodynamic accelerators are any linear accelerator and cyclotron. The type of ions and energy levels is determined by the ion beam type.

Ion irradiation is being used over neutron irradiation for its high damage rates in a short amount of time and the ability to irradiated a material without activating it (as long as the ion energy is low enough). Section 2.1.2 discusses the use of ion irradiation over neutron in greater detail. Current test reactors in the United States can only reach up to 8 dpa/year and available world reactors can only reach up to 20 dpa/year [2]. Ions can produce similar cascades and defects as neutron irradiations in a much shorter time scale.

3.3.3 In situ facilities

TEM has the capability to see specimens at the atomic scale in real time. The TEM was first invented in 1933 and commercialized in 1939 [66]. Soon after concepts of in situ ion irradiation came into the circulation. The first in situ ion irradiation was done in 1961 with an oxidized tungsten filament [67]. Technology has since improved through installing a separate ion beam into the top column of the TEM to simultaneously observe the specimen while irradiating it with a separate ion. There are 12 in situ ion irradiation facilities worldwide with more planned to be built. The majority of in situ facilities are in Japan with the remaining in Russia, European Union and the United States.

In most in-situ ion beam cases, the ion beam enters the TEM above the sample port from an energy dispersive X-ray spectroscopy (EDS) port [65]. The beam then hits the specimen and exits the TEM column through a different port. Figure 1a. illustrates the beam entering the TEM column. Tilting the specimen and the angle the ion beam enters and hits the specimen depends on the facility being used.

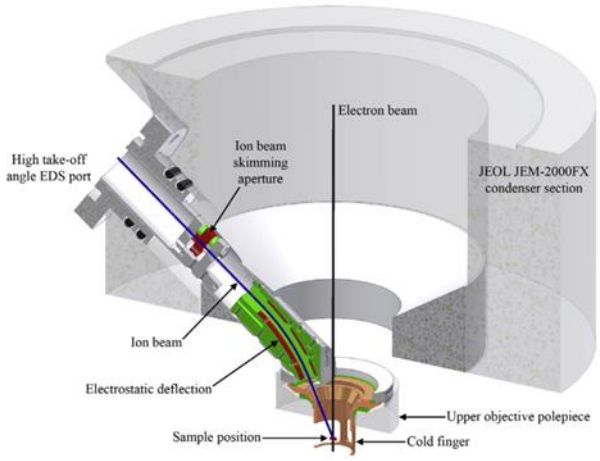

Figure 25. Ion beam entering the TEM and hitting the specimen [65].

The advantages of using ion in situ irradiation are studying live time damage events. The user can quantify damage as did Haley et al. [68]. Understanding live time damage events will lead to better simulations and computer codes to predict damage. Numerous groups including Kirk et al. are trying to use in situ ion irradiation to determined ion damage and relate it to neutron damage with computer modeling. [69].

The disadvantages of using in situ ion irradiation in a TEM include the size of the specimen, limited EDX capability and the free surfaces can serve as sinks for defects. Thin specimens have a large surface to volume ratio+ and surfaces are unsaturable defect sinks that are easily accessible to internal defects. One example is Haley et al [68] reported dislocation loops disappearing to the surface. EDX limitation is a disadvantage because analytical TEM such as irradiation induced segregation (and saturation of segregation) type of work is not possible during in-situ irradiation experiments. EDX is not available because the port the ion beam enters is the port that typically has EDX.

3.3.4 Sandia National Laboratories in situ ion irradiation TEM facility

Sandia National Laboratories (SNL) I^{3}TEM facility opened in 2010 and is funded by the Department of Energy and SNL. The major components of the I^{3}TEM facility can be seen in the figure below, and include a 200 kV JEOL 2100 high resolution TEM, a 6 MeV Tandem Van de Graaff–Pelletron accelerator, and a 10 kV Colutron G-1 ion accelerator [70].

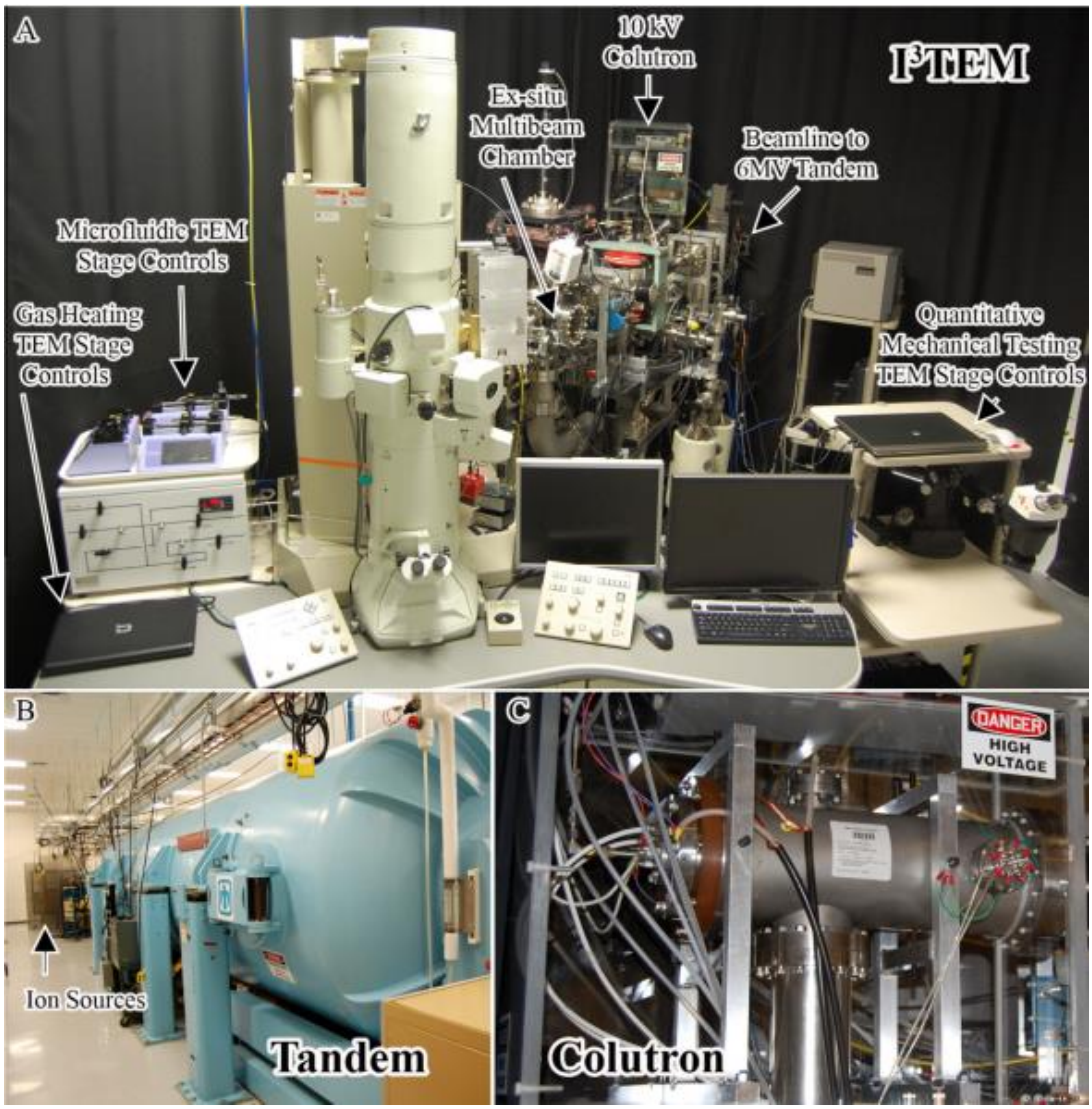

Figure 26. I^{3}TEM at SNL. (A) Capabilities and instrumentation the TEM (B) 6 MeV Tandem accelerator and ion source (C) 10 keV colutron accelerator [67]

The ion and ion energy vary widely with in situ TEM. The I^3TEM at Sandia National Labs allows for a wide range of ions and ion energies. The type of ion can range from hydrogen/protons up to heavier ions such as gold (Au). Most ions energies stay below 5 MeV but elements such as Si, Ni and Au can reach higher (10's of MeV) energies [67]. The wide range of ions and ion energies allow for a vast amount of experiments with different damage rate and productions.

3.3 Experimental Design

While undergoing preventative maintenance at the LANSCE IPF, the investigation of the Alloy 718 beam window showed formation of of γ" precipitates in certain regions close to outer ring. Both γ' and γ" precipitates are known to be unstable under irradiation conditions. The experiments which were conducted in this study were to understand the formation of γ" precipitates. To observe precipitation formation, the TEM technique of electron diffraction pattern was used. Under TEM in situ ion irradiation, the formation of precipitates could be chronicled if formation of the precipitate occurred. The experiments were conducted at the I^3TEM facility at SNL. Specimens were twin jet electro polished at LANL before the experiment at SNL. The first experiment was Ni ion in situ irradiation. The goal of the first test was to see if dose at room temperature will cause the formation of γ" precipitates. The second experiment was Au ion in situ irradiation at 200 ºC. The goal of the second test was to see if a combination of dose and an elevated temperature would promote an environment for γ" precipitates formation. The third experiment used proton in

situ irradiation. The goal of the proton irradiated test was to simulate the environment of the ion beam window portion which had γ" precipitates formed during irradiation.

CHAPTER 4: RESULTS

4.1 Computational Results

Computational analysis was conducted to estimate the dpa, range and energy deposited into Alloy 718. MCNP and SRIM were the two programs used. The section below discusses the computation results. How the codes work discussed in Chapter 2.

4.1.1 SRIM

The Stopping Range in Matter (SRIM) computer code can simulate ion and proton irradiation into a material. To conduct dose calculation, range and energy deposited a few assumptions were made as to follow Stoller et al.[52]. The SRIM calculations used the "quick" K-P method along with 0 eV for surface and lattice energies. The displacement energy was set at 40 eV [31]. SRIM does not take into effect recombination of defects and atoms. For all SRIM calculations the following material composition was used in Table 4.

Table 4. Material Input for SRIM.

Element	Atomic %
Ni	52
Fe	22
Cr	17
Nb	2.5
Ta	2.5
Mo	3
Co	1

Elements such as C, P, B, Si and Cu were omitted because of the low initial amounts and known impurities. Each simulation ran for 1e6 particles. All samples used the first 200 nm of the material to roughly estimate the TEM specimen. The first 200 nm was used to roughly estimate when the specimen is tilted 30º in the TEM holder. The calculations ran 10e6 particles.

4.1.1.1 SRIM Results for Ni ion irradiation

The dose calculated for 1.2 MeV nickel ions into Alloy 718 used a maximum depth of 650 nm. Figure 23 is the range and dose rate of 1.2 MeV Ni^{+2} ions in Alloy 718. The flux for Ni ion irradiation was calculated to be 7.5x10^{11} $\frac{ions}{cm^2 s}$.

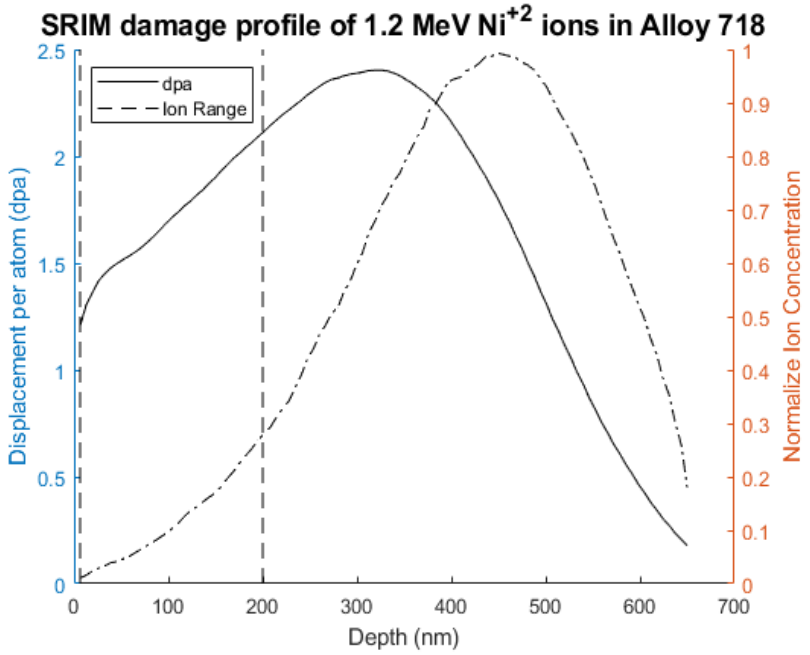

Figure 27. Dose rate and ion range of 1.2 MeV Ni ions into Alloy 718.

The average range of 1.2 MeV Ni ions in Alloy 718 is about 500 nm. The dose calculated to the specimen for 37 minutes of irradiation was 1.7 dpa. The energy deposited was calculated and plotted in Figure 27. The average ionization, for the first 200 nm, was calculated to be 166 eV/ Å-ion. The dominate transfer of energy is by ionization for the

first 200 nm. The vertical dotted lines in the plot above represents the 200 nm thick TEM foil region.

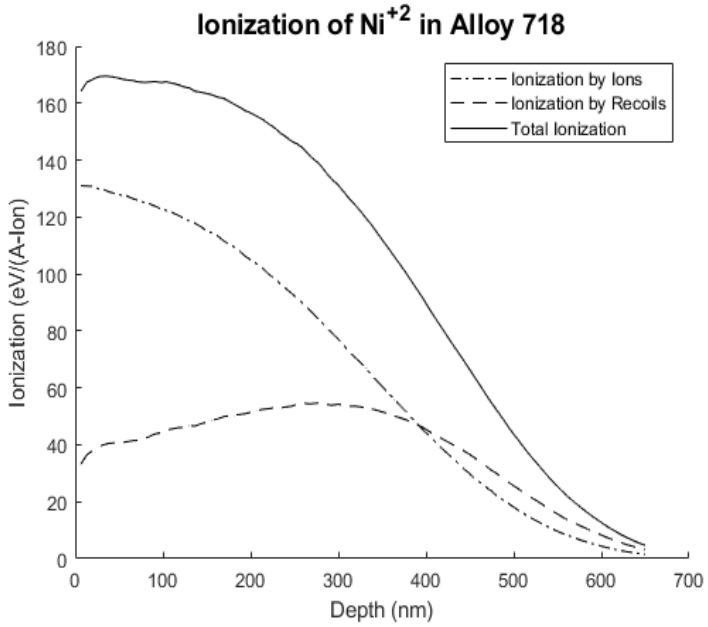

Figure 28. Ionization of Ni ions in Alloy 718.

4.1.1.2 SRIM Results for Au ion irradiation

The dose rate was calculated for 2.7 MeV gold ions into Alloy 718 at a depth of 450 nm. The dose was average to be 0.85 dpa for the first 200 nm (the thickness of the TEM foil) for an irradiation time of 54 minutes. The flux for Au ion irradiation was calculated to be $5x10^{10}\ \frac{ions}{cm^2 s}$.

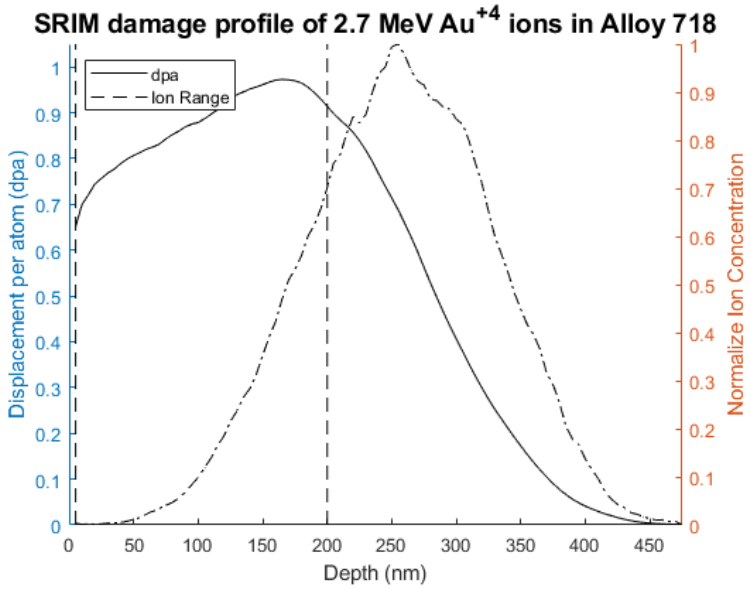

Figure 29. Dose rate and ion range of 2.7 MeV Au ions into Alloy 718

The average range of the ion was about 275 nm into the material. The average amount of energy deposited per Å is about 580 eV/ Å -ion for the first 2000 Å. Figure 26, describes the energy being deposited. The vertical dotted lines in the plot above represents the 200 nm TEM foil region.

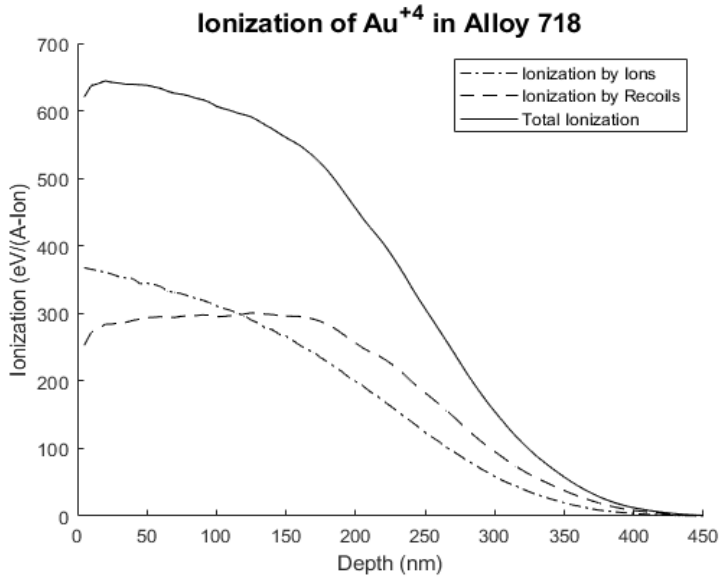

Figure 30. Ionization of Au ions in Alloy 718.

4.1.1.3 SRIM Results for Proton ion irradiation

The dose for 800 keV protons into Alloy 718 was calculated using a depth of 5,500 nm. The dose was averaged to be 0.023 dpa for the first 200 nm thickness of the TEM foil. The fluence for proton irradiation was averaged to be 1.8 x 10^{12} $\frac{ions}{cm^2 s}$. Figure 27 shows the damage and ion range as a function of depth.

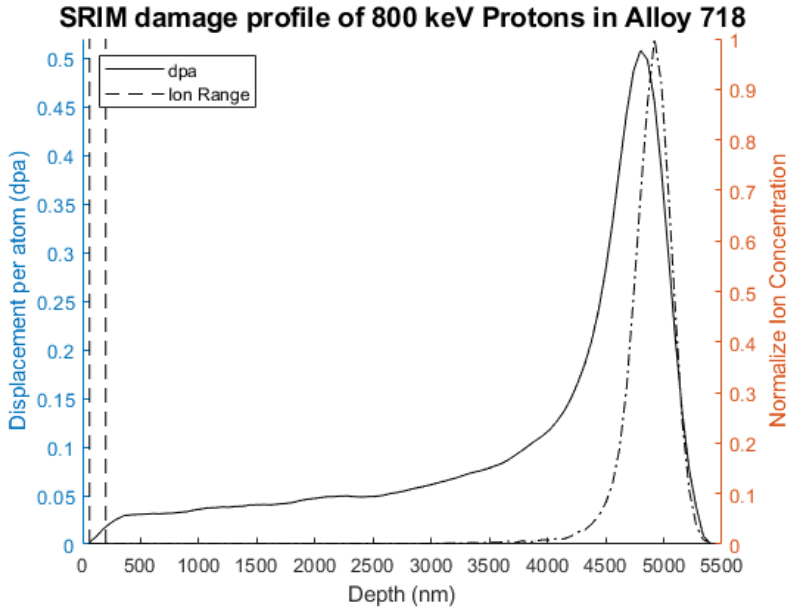

Figure 31. Dose rate and ion range of 800 keV protons into Alloy 718.

The range of the ion was about 5000 nm into the material. The energy deposited per Å is averaged to be 11.8 eV/ Å -ion. The ionization of protons in Alloy 718 is shown in Figure 32. Protons are predominantly slowed down by Coulomb interactions. The vertical dotted lines in the plot above represents the 200 nm TEM foil region.

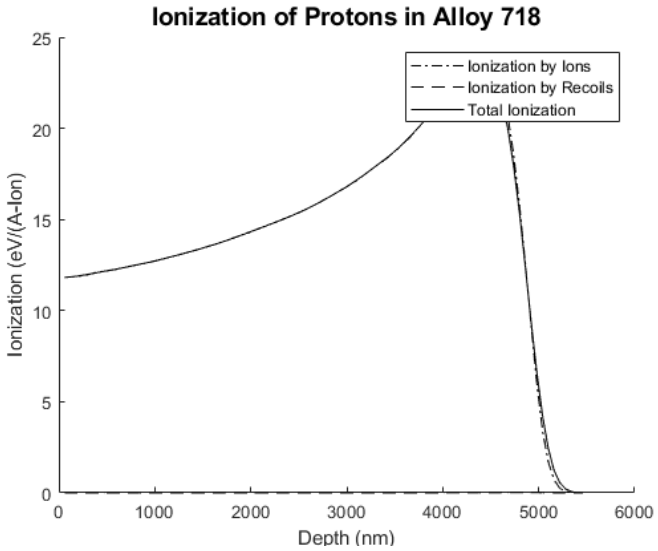

Figure 32. Ionization of protons in Alloy 718.

4.2 Ion in situ Irradiation

The goal of testing solution annealed Alloy 718 under irradiation environments is to simulate the Los Alamos Neutron Science Center (LANSCE) Isotope Production Facility (IPF) ion beam window to further understand the formation mechanism of γ" precipitates. A previous study by Bach et al. found at about 0.7 dpa and 33ºC γ" precipitates

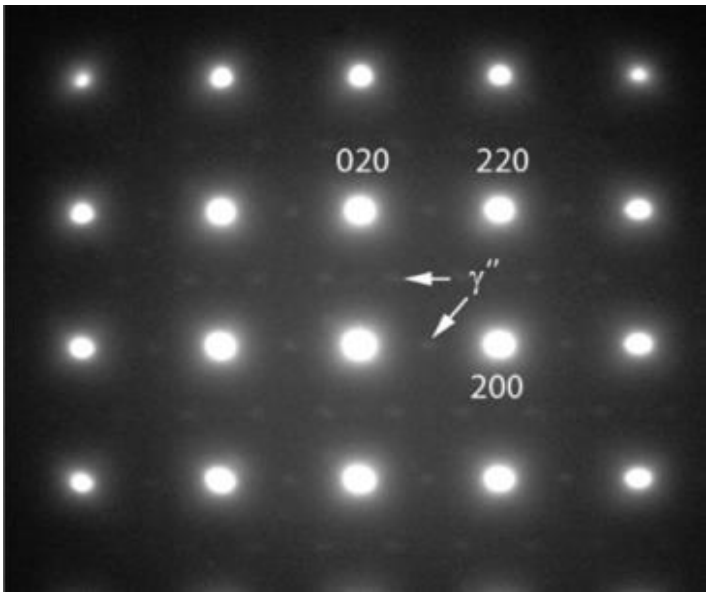

Figure 33. Diffraction pattern from Bach et al study of the SA Alloy 718 beam window.

formed in SA Alloy 718 [31]. Figure 30 shows the diffraction pattern from that study. The experiments were conducted at I^{3}TEM Facility at SNL with additional analysis done with the University of New Mexico 2010F JEOL TEM. The ion irradiation performed in situ with TEM tried to see and quantify any formation of γ" precipitates formed. The formation of γ" precipitates will be quantified by the intensity of the superlattice beam spot in the diffraction pattern in the [001] zone axis.

4.2.1 in situ Nickel Irradiation

Nickel ion irradiation was used to create higher amounts of radiation damage. In Figure 31, the before and after SADP in [001] direction is shown. No indication of superlattice spots from γ" precipitates are visible. No SADP's were taken during irradiation. The maximum dpa calculated using SRIM was 1.7 dpa.

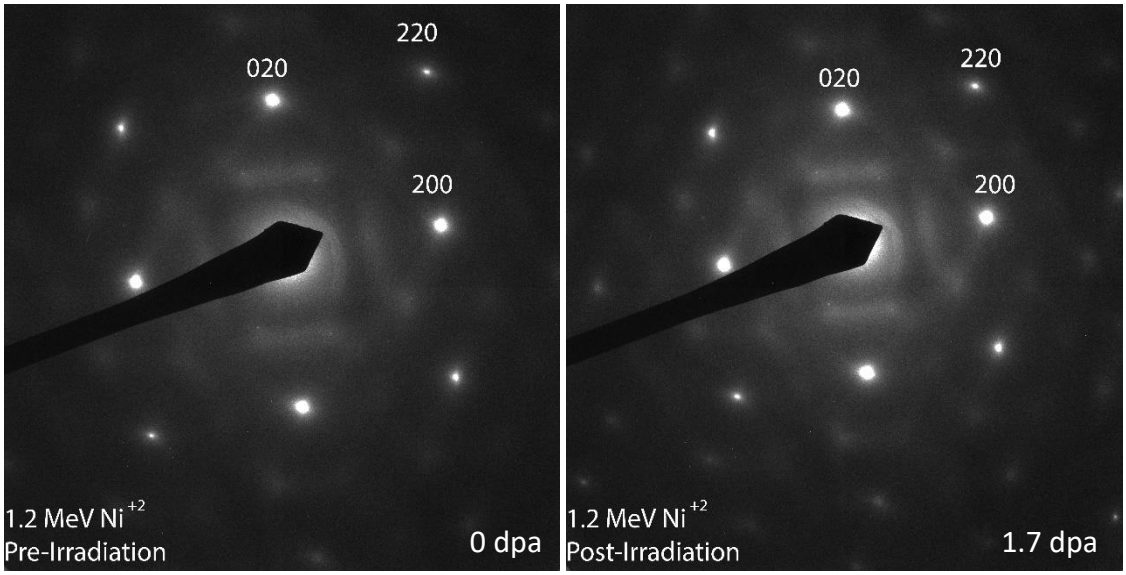

Figure 34. Ni ion irradiated SADP

Contrast plots were created using ImageJ as shown in Figure 32. The contrast plots show no signs super lattice patterns.

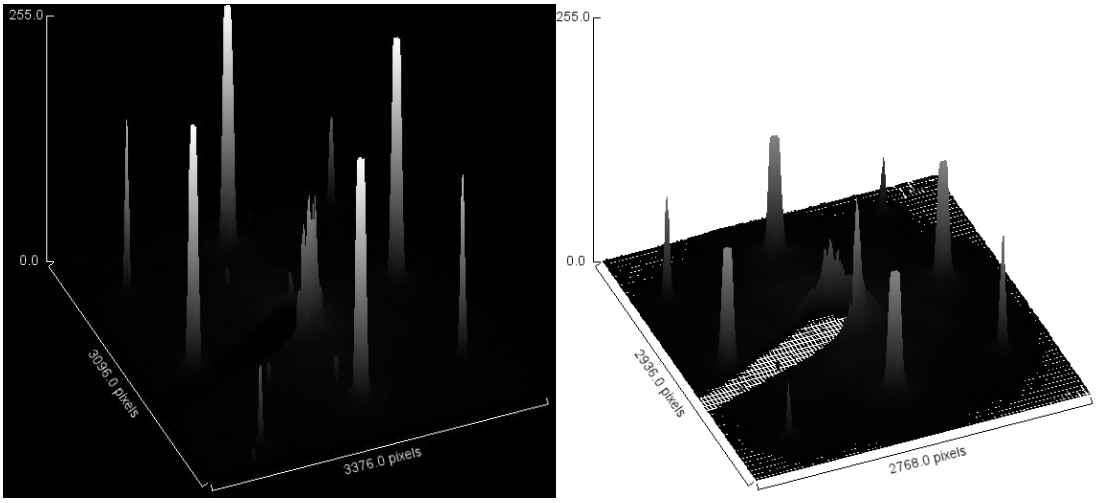

Figure 35. (Left) pre-irradiation contrast plot. (Right) Post-irradiation contrast plot.

4.2.2 in situ Gold Ion Irradiation

Gold ion irradiation was conducted on an Alloy 718 sample at a temperature of 200 ºC. The maximum dpa was calculated to be 0.85 dpa. During the irradiation a SADP image was taken at the beginning, then at 20 minutes and every 30 seconds after. The first 20 minutes of irradiation was not captured because of technical difficulties.

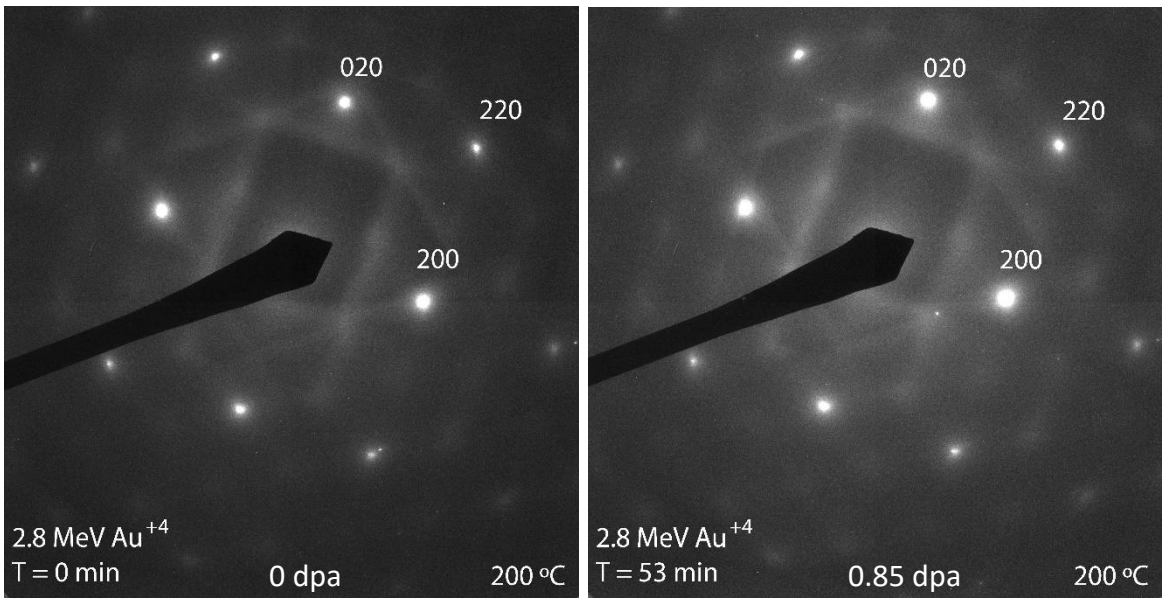

Figure 36 Au ion irradiated SADP

Contrast plots were created using ImageJ as shown in Figure 34. The contrast plots show that no signs of super lattice patterns were detected.

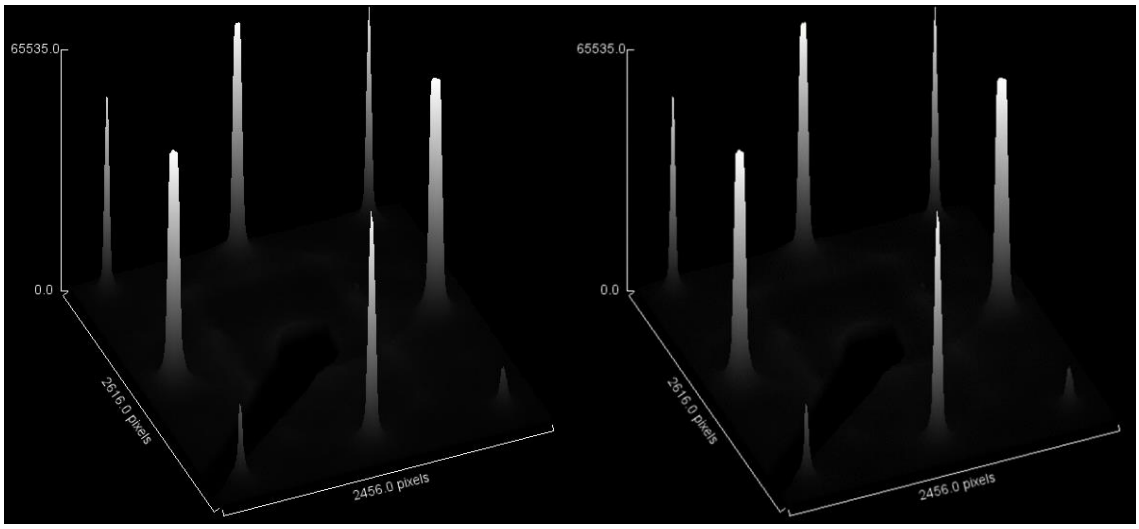

Figure 37 (Left) pre-irradiation contrast plot. (Right) Post-irradiation contrast plot.

4.2.3 in situ proton Irradiation

Proton irradiation was conducted at room temperature. The irradiation time was 64 hours. The last SADP taken at SNL occurred 12 hours into the experiment. Post analysis

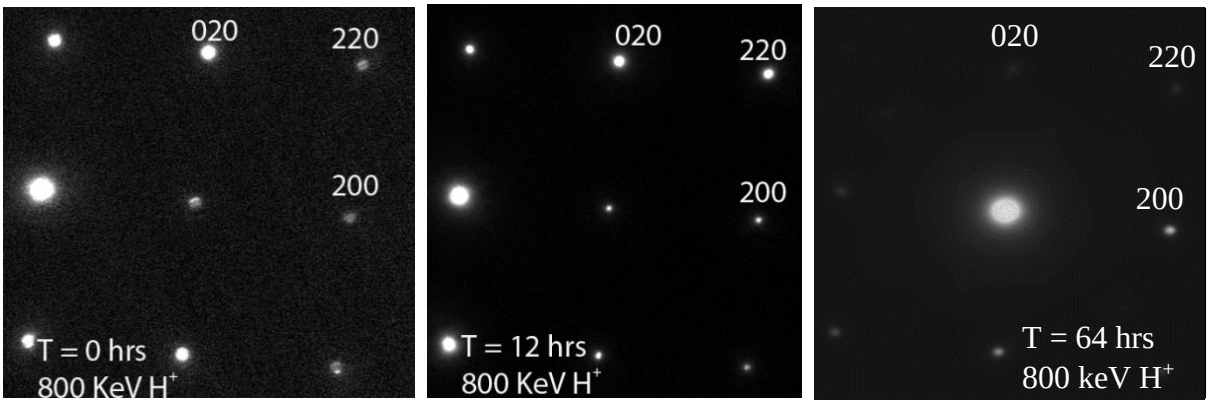

Figure 38. Proton irradiation SADP

was conducted at the UNM TEM facility. In Figure 38, the SADP for pre- irradiation, 12 hours into irradiation and post analysis do not indicate any formation of precipitates.

Contrast plots were created using ImageJ as shown in Figure 36. The contrast plots show no signs super lattice patterns.

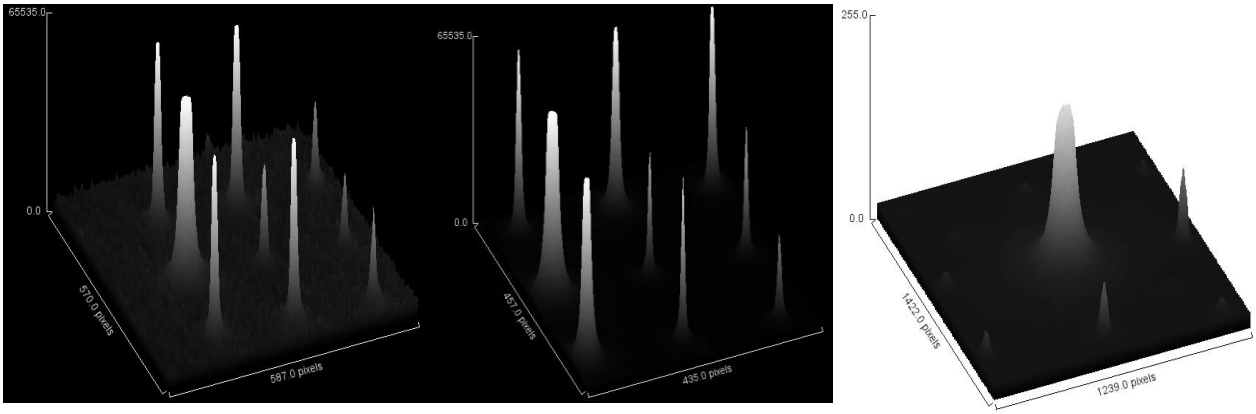

Figure 39. (Left) pre-irradiation contrast plot. Middle contrast plot after 12 hours of irradiation. (Right) Post-irradiation contrast plot.

The current of the beam was measured throughout the experiment. Figure 37 plots the current as a function of time. Around 24 hours into irradiation, the ion beam was block from the sample to try to fix the TEM.

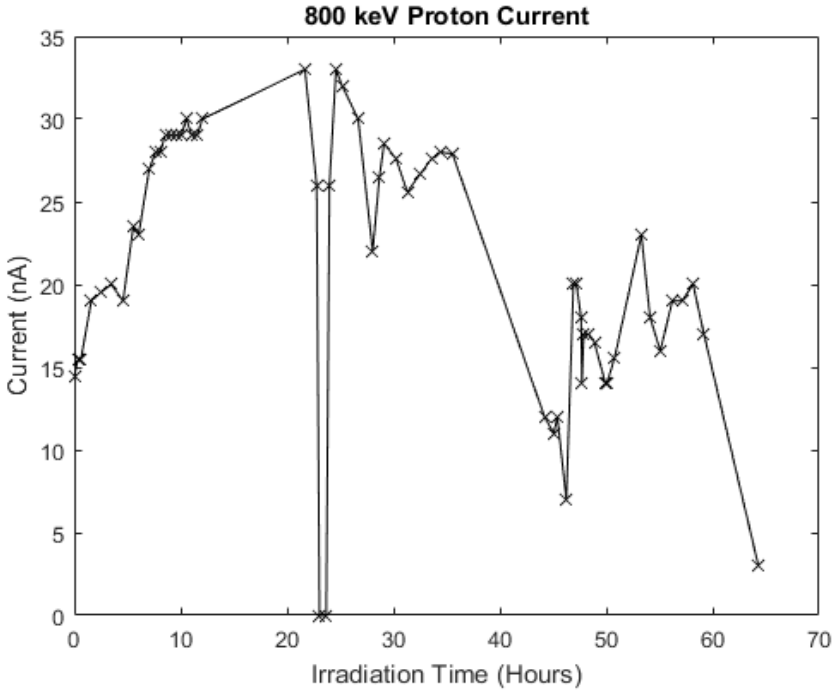

Figure 40. Current (nA) readings thoughout the test

4.3 Ion Beam Window Stress Analysis

Following the null results of *in situ* irradiation, the search to find another possible reason for precipitate growth was needed. A study by Qin et al. [47] suggested γ" precipitates are aided by external stresses on the material.

The thermal stress of the ion beam was calculated using equation 12, 13, and 14 from Chapter 2. To calculate the thermal stress, the following variables were used, E = 208 GPa, $\alpha = 13 \times 10^{-6}$ mm/(m-ºC) and an assumed ΔT to be 100 ºC. The thermal stress induced across the temperature difference was calculated to be 0.27 MPa. This value is not in the

same order of magnitude at which Qin et al [47] used in aging the specimens. Since the thermal stress was not the same order of magnitude, external force caused by the difference in pressure was calculated using Solidworks.

Solidworks was used to estimate the stress acting upon the ion beam window during normal operations. Properties listed in Chapter 3 were used to describe the alloy in Solidworks. The average atmospheric pressure at Los Alamos, 82 kPa, was used in the

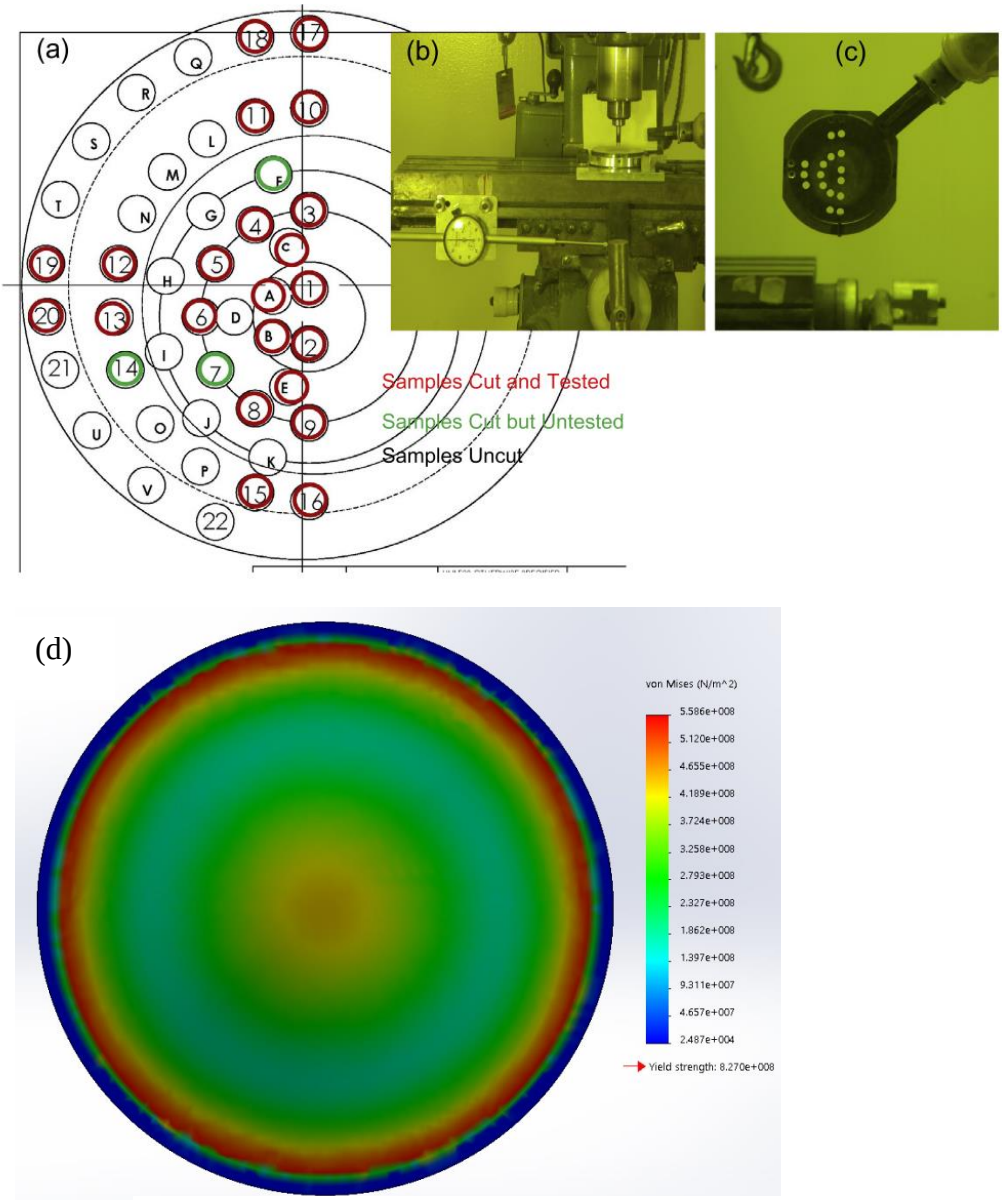

Figure 41. Ion beam widow cutting plan [31] *(a); Mill machine with special tungsten cutting bit at the Chemical and Metallurgical Research (CMR) LANL facility (b); view of the cutouts of the ion beam window (c); Solidworks stress profile of LANSCE IPF ion beam window (d).*

model along with a perfect vacuum of -82 kPa was assumed to be on one. Linear Elastic Isotropic Model was used for the Solidworks calculations. The maximum stress calculated was 550 MPa. The maximum stress was seen in the outer area of the ion beam window. In Figure 41a, sample 19 had γ" precipitates form in the window in the same area of maximum stress of the window. The stress across the ion beam window is in the same order of magnitude as Qin et al reported. The area where γ" precipitates formed had the lowest dose rate and highest external stress.

CHAPTER 5: CONCLUSIONS AND FUTURE WORK

5.1 In-situ Experiments

In-situ experiments conducted SNL concluded that no precipitates were observed induced by irradiation. Formation of γ" precipitates were discovered during the Ni, Au and proton irradiations of SA Alloy 718. SADP showed now indication of γ" precipitates formation. The test concluded ion irradiation of SA Alloy 718 with dose rates of 0.028 to 1.7 dpa does not induce γ" precipitates.

5.2 Stress Analysis

SolidWorks stress analysis concluded the maximum stress occurred at the outer area of the ion beam where the γ" precipitates were discovered. The maximum stress calculated was 556 MPa. The maximum stress is on the same order of magnitude as previous literature work showing gamma double prime formation. The SolidWorks stress analysis along with Qin et al study suggests the γ" precipitates form under stress. Qin et al study went up to higher temperatures than the calculated temperature of the ion beam. The irradiation and stress conditions could create an environment for γ" precipitates growth.

5.3 Future Work

Recent publication suggests the formation of γ" precipitates is aided by external stress applied to the material during the anneal process [47]. Future work should investigate the relation of stress applied to the material and dose of the material.

REFERENCES

[1] S. Chu, A. Majumdar, Opportunities and challenges for a sustainable energy future, Nature. 488 (2012) 294–303. doi:10.1038/nature11475.

[2] S.J. Zinkle, J.T. Busby, Structural materials for fission & fusion energy, Mater. Today. 12 (2009) 12–19. doi:http://dx.doi.org/10.1016/S1369-7021(09)70294-9.

[3] K.L. Murty, I. Charit, Structural materials for Gen-IV nuclear reactors: Challenges and opportunities, (n.d.). doi:10.1016/j.jnucmat.2008.08.044.

[4] S.J. Zinkle, G.S. Was, Materials challenges in nuclear energy, Acta Mater. 61 (2013) 735–758. doi:10.1016/j.actamat.2012.11.004.

[5] F. Cattant, D. Crusset, D. Féron, M. Stan, E.A. Marquis, J.M. Hyde, D.W. Saxey, S. Lozano-Perez, V. de Castro, D. Hudson, C.A. Williams, S. Humphry-Baker, G.D.W. Smith, T. Allen, J. Busby, M. Meyer, D. Petti, Materials challenges for nuclear systems, Mater. Today. 12 (2009) 30–37. doi:10.1016/S1369-7021(09)70295-0.

[6] E.A. Marquis, J.M. Hyde, D.W. Saxey, S. Lozano-Perez, V. De Castro, D. Hudson, C.A. Williams, S. Humphry-Baker, G.D.W. Smith, Nuclear reactor materials at the atomic scale, Mater. Today. 12 (2009). doi:10.1016/S1369-7021(09)70296-2.

[7] S. Zhou, X. Zhang, Nuclear energy development in China: A study of opportunities and challenges, (2010). doi:10.1016/j.energy.2009.04.020.

[8] N. Armaroli, V. Balzani, The future of energy supply: Challenges and opportunities, Angew. Chemie - Int. Ed. 46 (2007) 52–66. doi:10.1002/anie.200602373.

[9] Y. Guérin, G.S. Was, S.J. Zinkle, Materials Challenges for Advanced Nuclear Energy Systems, (n.d.). doi:10.1017/S0883769400100028.

[10] T. Alen, J. Busby, M. Meyer, D. Petti, Material challenges for nuclear systems, Mater. Today. 13 (2010) 14–23. doi:10.1016/S1369-7021(09)70294-9.

[11] The Institution of Electrical Engineers, Nuclear Reactor Types, Iee. (2005) 1–15. doi:ISBN 0 85296 581 8.

[12] IAEA, Thermophysical Properties of Materials for Nuclear Engineering: A Tutorial and Collection of Data, At. Energy. (2008) 200. doi:http://dx.doi.org/10.1002/cbdv.200490137.

[13] S.A. Maloy, M.R. James, G. Willcutt, W.F. Sommer, M. Sokolov, L.L. Snead, M.L. Hamilton, F. Garner, The mechanical properties of 316L/304L stainless steels, Alloy 718 and Mod 9Cr-1Mo after irradiation in a spallation environment, J. Nucl. Mater. 296 (2001) 119–128. doi:10.1016/S0022-3115(01)00514-1.

[14] T.R. Allen, J.I. Cole, E.A. Kenik, Radiation-Induced Segregation and Void Swelling in 304 Stainless Steel, in: Eff. Radiat. Mater. 20th Int. Symp., ASTM

STP 1405, 2001: pp. 433–448. https://www.osti.gov/servlets/purl/757550 (accessed February 19, 2018).

[15] S.M. Bragg-Sitton, Presentation: Update on Accident Tolerant Fuel and IAEA Technical Meeting on ATF Accident Tolerant Fuel (ATF) Goal : Enhanced " Grace Time ," Idaho Natl. Lab. (2015). https://www.iaea.org/OurWork/ST/NE/NEFW/Technical-Areas/NFC/documents/TWGFPT/2015/Presentations/(12)_ATF_update_and_TM.pdf (accessed February 21, 2018).

[16] S. Ray, S.C. Johnson, E.J. Lahoda, Preliminary Assessment of the Performance of SiC Based Accident Tolerant Fuel in Commercial LWR Systems, 2013. http://www.westinghousenuclear.com/Portals/0/about/reports/Additional December 2015/Preliminary Assessment of the Performance of SiC Based Accident Tolerant Fuel in Commercial LWR Systems.pdf (accessed February 21, 2018).

[17] S.M. Bragg-sitton, Advanced Fuels Campaign: Light Water Reactor Accident Tolerant Fuel Performance Metrics, U.S. Dep. Energy Adv. Fuels Campaign. (2014). https://nuclearfuel.inl.gov/atf/Reports/ATF Metrics Report Feb 2014.pdf (accessed February 21, 2018).

[18] J. Buongiorno, U.S. Scwr, P. Manager, P.E. Macdonald, Supercritical Water Reactor (SCWR) Progress Report for the FY-03 Generation-IV R&D Activities for the Development of the SCWR in the U.S, (2003). http://nuclear.inel.gov/gen4/docs/scwr_annual_progress_report_gen-iv_fy-03.pdf (accessed February 19, 2018).

[19] J.R. LaMarsh, A.J. Baratta, Introduction to Nuclear Engineering, 3rd Edtion, 2001.

[20] Status Report – MSR-FUJI, (2000). https://aris.iaea.org/PDF/MSR-FUJI.pdf (accessed February 19, 2018).

[21] R. Stainsby, The Generation IV Gas Cooled Fast Reactor, GoFastR Present. 44 (n.d.). https://www.iaea.org/INPRO/cooperation/5th_GIF_Meeting/GFR_Stainsby.pdf (accessed February 19, 2018).

[22] G. Was, Fundamentals of Radiation Materials Science, 2007. doi:10.1007/978-3-540-49472-0.

[23] M.K. Miller, T.F. Kelly, K. Rajan, S.P. Ringer, The future of atom probe tomography, Mater. Today. 15 (2012) 158–165. doi:10.1016/S1369-7021(12)70069-X.

[24] Inconel 718 Spec Sheet from Special Materials, (n.d.). http://www.specialmetals.com/assets/smc/documents/inconel_alloy_718.pdf (accessed February 20, 2018).

[25] R.B. Bhavsar, A. Collins, S. Silverman, Use of alloy 718 and 725 in oil and gas industry, Superalloys 718, 625, 706 Var. Deriv. (2001) 47–55.

doi:10.7449/2001/Superalloys_2001_47_55.

[26] A. Devaux, L. Nazé, R. Molins, A. Pineau, A. Organista, J.Y. Guédou, J.F. Uginet, P. Héritier, Gamma double prime precipitation kinetic in Alloy 718, Mater. Sci. Eng. A. 486 (2008) 117–122. doi:10.1016/j.msea.2007.08.046.

[27] B.H. Sencer, G.M. Bond, F.A. Garner, M.L. Hamilton, B.M. Oliver, L.E. Thomas, S.A. Maloy, W.F. Sommer, M.R. James, P.D. Ferguson, Microstructural evolution of Alloy 718 at high helium and hydrogen generation rates during irradiation with 600-800 MeV protons, J. Nucl. Mater. 283–287 (2000) 324–328. doi:10.1016/S0022-3115(00)00308-1.

[28] A. Krása, A.K. Rež, Spallation Reaction Physics, (2010). http://ojs.ujf.cas.cz/~krasa/ZNTT/SpallationReactions-text.pdf (accessed January 19, 2018).

[29] L. Thomas, S. Bruemmer, Radiation-Induced Mircostructural Evolution and Phase Stability in Nickel-Base Alloy 718, Proc. Eigth Interntional Symp. Environ. Degrad. Mater. Nucl. Power Syst. - Water React. 2 (1997) 772–779.

[30] B.H. Sencer, G.M. Bond, F.A. Garner, M.L. Hamilton, S.A. Maloy, W.F. Sommer, Correlation of radiation-induced changes in mechanical properties and microstructural development of Alloy 718 irradiated with mixed spectra of high-energy protons and spallation neutrons, in: J. Nucl. Mater., 2001: pp. 145–154. doi:10.1016/S0022-3115(01)00517-7.

[31] H.T. Bach, O. Anderoglu, T.A. Saleh, T.J. Romero, C.T. Kelsey, E.R. Olivas, B.H. Sencer, P.O. Dickerson, M.A. Connors, K.D. John, S.A. Maloy, Proton irradiation damage of an annealed Alloy 718 beam window, J. Nucl. Mater. 459 (2015) 103–113. doi:10.1016/j.jnucmat.2014.12.096.

[32] R.. Nelson, J.. Hudson, D.J. Mazey, The stability of precipitates in an irradiation environment, J. Nucl. Mater. 44 (1972) 318–330.

[33] F. Bourdeau, E. Camus, C. Abromeit, H. Wollenberger, Disordering and dissolution of y' precipitates under ion irradiation, Phys. Rev. B. 50 (1994) 205–211. https://journals.aps.org/prb/pdf/10.1103/PhysRevB.50.16205 (accessed June 16, 2017).

[34] H.K. Zhang, Z. Yao, M.A. Kirk, M.R. Daymond, Stability of Ni3(Al, Ti) gamma prime precipitates in a nickel-based superalloy inconel X-750 under heavy ion irradiation, Metall. Mater. Trans. A Phys. Metall. Mater. Sci. 45 (2014) 3422–3428. doi:10.1007/s11661-014-2309-y.

[35] S. Jin, F. Luo, S. Mab, J. Chen, T. Li, R. Tang, L. Guo, Evolution of precipitate in nickel-base alloy 718 irradiated with argon ions at elevated temperature, Nucl. Instruments Methods Phys. Res. Sect. B Beam Interact. with Mater. Atoms. 307 (2013) 522–525. doi:10.1016/j.nimb.2012.12.105.

[36] T.S. Byun, K. Farrell, Tensile properties of Inconel 718 after low temperature neutron irradiation, in: J. Nucl. Mater., 2003: pp. 292–299. doi:10.1016/S0022-

3115(03)00006-0.

[37] W.G. Wolfer, Fundamental properties of defects in metals, Elsevier Inc., 2012. doi:10.1016/B978-0-08-056033-5.00001-X.

[38] F. Agullo-Lopez, C.R.A. Catlow, P.D. Townsend, Point Defects in Materials, Acad. Press. (1988) 445.

[39] M.R. James, S.A. Maloy, F.D. Gac, W.F. Sommer, J. Chen, H. Ullmaier, The mechanical properties of an Alloy 718 window after irradiation in a spallation environment, in: J. Nucl. Mater., 2001: pp. 139–144. doi:10.1016/S0022-3115(01)00516-5.

[40] J.. Hunn, E.. Lee, T.. Byun, L.. Mansur, Ion-irradiation-induced hardening in Inconel 718, J. Nucl. Mater. 296 (2001) 203–209. doi:10.1016/S0022-3115(01)00519-0.

[41] G.S. Was, R.S. Averback, Radiation damage using ion beams, Elsevier Inc., 2012. doi:10.1016/B978-0-08-056033-5.00007-0.

[42] G.S. Was, Challenges to the use of ion irradiation for emulating reactor irradiation, J. Mater. Res. 30 (2015) 1158–1182. doi:10.1557/jmr.2015.73.

[43] A. Baldan, Review Progress in Ostwald ripening theories and their applications to nickel-base superalloys Part I: Ostwald ripening theories, 3 (n.d.) 2171–2202. http://www.eng.uc.edu/~beaucag/Classes/Nanopowders/Ostwald Ripening Rate Theories (LSW).pdf (accessed April 10, 2018).

[44] W.D. Callister, D.G. Rethwisch, Material Science and Engineering an Introduction, n.d.

[45] J.F. Shackelford, Introduction to Material Science for Engineers, Macmillan Publishing Company, 1992.

[46] S.T. Wlodek, R.D. Field, The Effects of Long Time Exposure on Alloy 718, Superalloys 718, 625, 706 Deriv. E.A. Loria Ed., TMS. (1994) 659–670. doi:10.7449/1994/Superalloys_1994_659_670.

[47] H. Qin, Z. Bi, H. Yu, G. Feng, J. Du, J. Zhang, Influence of stress on γ″ precipitation behavior in Inconel 718 during aging, J. Alloys Compd. 740 (2018) 997–1006. doi:10.1016/j.jallcom.2018.01.030.

[48] J.H. Ke, H. Ke, G.R. Odette, D. Morgan, Cluster dynamics modeling of Mn-Ni-Si precipitates in ferritic-martensitic steel under irradiation, J. Nucl. Mater. 498 (2018) 83–88. doi:10.1016/j.jnucmat.2017.10.008.

[49] J.L. Klatt, R.S. Averback, D. Peak, J.L. Klatt, R.S. Averback, Ion Beam Mixing in Ag-Pd Alloys Ion beam mixing in Ag .. Pd aUoys, Appl. Phys. Lett. 553 (1989). doi:10.1063/1.101637.

[50] J.F. Ziegler, J.P. Biersack, M.D. Ziegler, -SRIM- The Stopping and Range of Ions in Matter(2008), (2008).

[51] J.P. Biersack, Computer simulations of sputtering, Nucl. Instruments Methods Phys. Res. Sect. B Beam Interact. with Mater. Atoms. 27 (1987) 21–36.

[52] R. Stoller, M. Toloczko, G. Was, A. Certain, S. Dwaraknath, F. Garner, On the use of SRIM for computing radiation damage exposure, Nucl. Inst. Methods Phys. Res. B. 310 (2013) 75–80. doi:10.1016/j.nimb.2013.05.008.

[53] N. Hashimoto, J.D. Hunn, T.S. Byun, L.K. Mansur, Microstructural analysis of ion-irradiation-induced hardening in inconel 718, J. Nucl. Mater. 318 (2003) 300–306. doi:10.1016/S0022-3115(03)00013-8.

[54] M. Sundararaman, S. Banerjee, H. Mori, The Stability of γ" and γ' phases in Alloy 718 under electron irradiation, Superalloys 718, 625, 706 Var. Deriv. 19 (2001) 379–387. doi:10.7449/2001/Superalloys_2001_379_387.

[55] F. Carsughi, H. Derz, P. Ferguson, G. Pott, W. Sommer, H. Ullmaier, Investigations on Inconel 718 irradiated with 800 MeV protons, J. Nucl. Mater. 264 (1999) 78–88. doi:10.1016/s0022-3115(98)00475-9.

[56] C. Sun, M. Kirk, M. Li, K. Hattar, Y. Wang, O. Anderoglu, J. Valdez, B.P. Uberuaga, R. Dickerson, S.A. Maloy, Microstructure, chemistry and mechanical properties of Ni-based superalloy Rene N4 under irradiation at room temperature, Acta Mater. 95 (2015) 357–365. doi:10.1016/j.actamat.2015.04.061.

[57] H.K. Zhang, Z. Yao, G. Morin, M. Griffiths, TEM characterization of in-reactor neutron irradiated CANDU spacer material Inconel X-750, J. Nucl. Mater. 451 (2014) 88–96. doi:10.1016/j.jnucmat.2014.03.043.

[58] R. Polvorosa, A. Suárez, L.N.L. de Lacalle, I. Cerrillo, A. Wretland, F. Veiga, Tool wear on nickel alloys with different coolant pressures: Comparison of Alloy 718 and Waspaloy, J. Manuf. Process. 26 (2017) 44–56. doi:10.1016/J.JMAPRO.2017.01.012.

[59] International Molybdenum Association, Applications of Mo Metal and Its Alloys, 2013. www.imoa.info (accessed March 8, 2018).

[60] A. Lingenfelter, WELDING OF INCONEL ALLOY 718: A HISTORICAL OVERVIEW, (n.d.). http://www.tms.org/Superalloys/10.7449/1989/Superalloys_1989_673_683.pdf (accessed February 20, 2018).

[61] W.C. Oliver, G.M. Pharr, An improved technique for determining hardness and elastic modulus using load and displacemnt sensing indentation experiments, Mater. Res. 7 (1992) 1564–1583.

[62] D.V.S. Rao, K. Muraleedharan, C.J. Humphreys, TEM specimen preparation techniques, Microsc. Sci. Technol. Appl. Educ. (2010) 1232–1244. doi:10.1007/BF02645554.

[63] L. Reimer, Transmission electron microscopy : physics of image formation, 5th ed., Springer, New York, NY, 2008.

[64] D. William, C. Carter, Transmission Electron Microscopy: A Textbook For Materials Science, Springer, New York, USA, n.d.

[65] J.A. Hinks, A review of transmission electron microscopes with in situ ion irradiation, Nucl. Instruments Methods Phys. Res. Sect. B Beam Interact. with Mater. Atoms. 267 (2009) 3652–3662. doi:10.1016/j.nimb.2009.09.014.

[66] E. Ruska, The Development of the Electron Microscope and Electron Microscopy, (1986). https://www.nobelprize.org/nobel_prizes/physics/laureates/1986/ruska-lecture.pdf (accessed December 8, 2017).

[67] K. Hattar, D.C. Bufford, D.L. Buller, Concurrent in situ ion irradiation transmission electron microscope, Nucl. Instruments Methods Phys. Res. Sect. B Beam Interact. with Mater. Atoms. 338 (2014) 56–65. doi:10.1016/j.nimb.2014.08.002.

[68] J.C. Haley, S.A. Briggs, P.D. Edmondson, K. Sridharan, S.G. Roberts, S. Lozano-Perez, K.G. Field, Dislocation loop evolution during in-situ ion irradiation of model FeCrAl alloys, (2017). doi:10.1016/j.actamat.2017.07.011.

[69] M.A. Kirk, M. Li, D. Xu, B.D. Wirth, Predicting neutron damage using TEM with in situ ion irradiation and computer modeling, J. Nucl. Mater. 498 (2018) 199–212. doi:10.1016/J.JNUCMAT.2017.10.023.

[70] Sandia Ion Beam Laboratory NSUF Partner Facilities Description, (n.d.).

[71] DOE-HDBK-1019/1-93, Nuclear Physics and Reactor Theory Volume 1 of 2, n.d.

[72] J. Knaster, A. Moeslang, T. Muroga, Materials research for fusion, (2016). doi:10.1038/NPHYS3735.

[73] M. Mozi, The Influence of Grain Size on the Mechanical Properties of Inconel 718, 2013. http://www.diva-portal.org/smash/get/diva2:779274/FULLTEXT01.pdf (accessed March 8, 2018).